# Development and application of a multi-scale modelling framework for urban high-resolution NO$_2$ pollution mapping

Zhaofeng Lv[1,★], Zhenyu Luo[1,★], Fanyuan Deng[1], Xiaotong Wang[1], Junchao Zhao[1], Lucheng Xu[1], Tingkun He[1],

Yingzhi Zhang[2], Huan Liu[1,*], Kebin He[1]

[1]State Key Joint Laboratory of ESPC, School of Environment, Tsinghua University, Beijing 100084, China

[2]College of Ecology and Environment, ChengDu University of Technology, Chengdu 610059, China

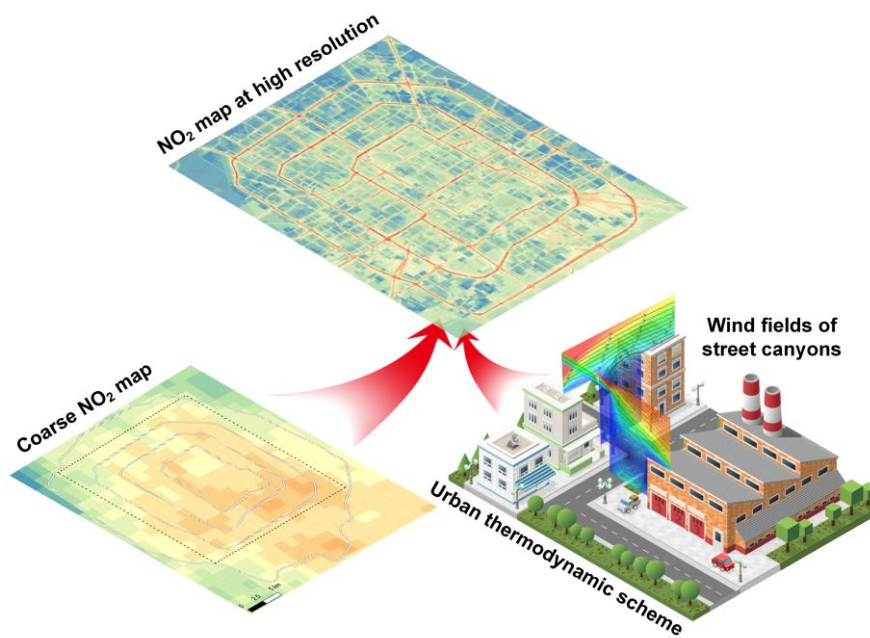[★] Z. Lv. and Z. Luo. contributed equally to this work.

Corresponding Author:

*Phone and fax: 86-10-62771679; e-mail: liu_env@tsinghua.edu.cn (Huan Liu)

**Abstract.** Vehicle emissions have become a major source of air pollution in urban areas, especially for near-road environments, where the pollution characteristics are difficult to be captured by a single-scale air quality model due to the complex composition of the underlying surface. Here we developed a hybrid model CMAQ-RLINE_URBAN to quantitatively analyse the effects of vehicle emissions on urban roadside NO$_2$ concentrations at a high spatial resolution of 50 m $\times$ 50 m. To estimate the influence of various street canyons on the dispersion of air pollutants, a Machine Learning-based Street Canyon Flow (MLSCF) scheme was established based on Computational Fluid Dynamic and two machine learning methods. The results indicated that compared with the CMAQ model, the hybrid model improved the underestimation of NO$_2$ concentration at near-road sites with MB changing from -10 μg/m$^3$ to 6.3 μg/m$^3$. The MLSCF scheme obviously increased upwind concentrations within deep street canyons due to changes in the wind environment caused by the vortex. In summer, the relative contribution of vehicles to NO$_2$ concentrations in Beijing urban areas was 39% on average, similar to results from CMAQ-ISAM model, but increased significantly with the decreased distance to the road centerline, especially reaching 75% on urban freeways.

25 **Graphical abstract.**



NO₂ map at high resolution

Coarse NO₂ map

Wind fields of street canyons

Urban thermodynamic scheme

26

## 1 Introduction

The accelerated urbanization leads to severe air pollution in China. As one of the indicators of air pollution, nitrogen dioxide ($NO_2$) causes an adverse impact on human health and promotes the generation of ozone and particulate matter (Pandey et al., 2005; Khaniabadi et al., 2017). During the last decade, benefiting from the implementations of several air pollution control strategies by the Chinese government, the air quality has improved (Jin et al., 2016; Zheng et al., 2018), and the vertical column densities of $NO_2$ displayed a decreasing trend after 2013 (Shah et al., 2020; Cui et al., 2021). However, the economic development and nitrogen oxides ($NO_x$) emissions are not decoupled in China (Luo et al., 2022a). In some megacities of China, such as Chengdu, the daily averaged $NO_2$ concentration could reach 200 $\mu g/m^3$ (Zhu et al., 2019), far exceeding the 24-h average air quality guideline of 80 $\mu g/m^3$ suggested by the Ministry of Environmental Protection of China.

The improvement of $PM_{2.5}$ in China was mainly due to the emission reduction and control measures of industrial and domestic sources (Zhang et al., 2019b), which also relieved the $NO_2$ pollution, but the reduction potential of these sources has been gradually declining. Meanwhile, as the population of vehicles is growing rapidly, vehicle emissions have become a major source of $NO_2$ pollution, especially in urban areas (Nguyen et al., 2018). Due to the low release height of vehicle emissions, combined with the negative dispersion condition caused by nearby buildings, air pollutants will be significantly accumulated near the street. According to roadside observations, within the distance of about 100-200 m near roads, the concentrations of CO, $NO_2$, ultrafine particulate matter (UFP), $PM_{2.5}$, $PM_{10}$, and other pollutants will increase with the decreased distance to the road centerline, especially for the pollution levels of $NO_2$ and UFP increasing exponentially. Therefore, the gradient of concentration around the road changes dramatically (Nayeb Yazdi et al., 2015; Hagler et al., 2012). Moreover, the dispersion of air pollutants in the near-road environment is significantly affected by geometric characteristics of the street canyon. For example, in a standard street canyon, when the external wind direction at the roof level is perpendicular to the street axis, a clockwise vortex will be generated inside, resulting in the accumulation of pollutant concentrations at the upwind grid receptors in the canyon (Oke, 1988; Manning et al., 2000). Consequently, how to quantitatively identify urban vehicle-induced air pollution around roads affected by complex underlying surface conditions has become an urgent scientific issue.

Regional-scaled air quality models, represented by Chemical Transport Models (CTMs) including Community Multi-scale Air Quality (CMAQ) model (Byun and Schere, 2006), Comprehensive Air quality Model with

57  extensions (CAMx), and Weather Research and Forecasting/Chemistry model (WRF-Chem) (Grell et al., 2005),

58  have been used extensively in assessment on the impacts of vehicle emissions on the regional atmospheric

59  environment, focusing on the source apportionment (Luo et al., 2022b; Vara-Vela et al., 2016; Kheirbek et al.,

60  2016; Lv et al., 2020) and evaluation of control measures (Zhang et al., 2020; Yu et al., 2019; Cheng et al., 2019;

61  Ke et al., 2017). However, the spatial resolution of CTMs is generally larger than 1 km×1 km, so the significant

62  impacts of vehicle emissions on near-source air quality cannot be predicted by CTMs due to the grid

63  homogenization on vehicle emissions.

64

65  To avoid the aforementioned disadvantages, the local-scaled numerical models based on Gaussian diffusion theory

66  or computational fluid dynamic (CFD) are adopted by numerous researches to study at a finer spatial resolution

67  (Zhang et al., 2021b; Patterson and Harley, 2019; Soulhac et al., 2012), including Research LINE-source Dispersion

68  Model (RLINE) (Snyder et al., 2013), Operational Street Pollution Model (OSPM), AERMOD (Cimorelli et al.,

69  2005),  and RapidAir® (Masey et al., 2018). However, the large uncertainties in predictions from Gaussian

70  dispersion models come from the provided meteorological conditions and background concentrations. The natural

71  logarithm function is usually used to characterize the vertical profile of wind speed in both the inertial and rough

72  sublayers, neglecting the influence of urban complex underlying surface compositions on the wind field (Cimorelli

73  et al., 2005; Masey et al., 2018; Snyder et al., 2013). Nevertheless, in standard and deep street canyons, the changes

74  of vertical wind profile cannot be described by the logarithmic form, otherwise the actual wind speed will be greatly

75  overestimated (Soulhac et al., 2008). Although the OSPM has performed a large number of comparisons with field

76  observations in shallow or standard street canyons, the validation of model performance in deep street canyons

77  with a large aspect ratio was still inadequate (Kakosimos et al., 2010). Moreover, OSPM overestimated the bottom

78  wind speed in a deep street canyon by about 10 times compared with the predictions from CFD, resulting in greatly

79  underestimating pollutant concentrations (Murena et al., 2009). Comparatively speaking, CFD model can

80  accurately simulate the air flow and pollutant concentration in complex street canyons, but the simulation domain

81  of CFD model is much smaller than the urban scale, and the influence of the long-term meteorological boundary

82  conditions cannot be considered.

83

84  Considering the respective strengths and limitations of regional models and local models, several studies have been

85  carried out on coupling of air quality models applicable to different scales (Ketzel et al., 2012; Stocker et al., 2012;

86  Lefebvre et al., 2013; Jensen et al., 2017; Kim et al., 2018; Mallet et al., 2018; Hood et al., 2018; Benavides et al.,

87  2019; Kamińska, 2019; Mu et al., 2022). Although these models performed accurately in near-road simulation, the

88  influence of street canyons is still hard to be considered. In some hybrid models (Stocker et al., 2012; Jensen et al.,

89  2017; Mallet et al., 2018), OSPM was still applied to calculate concentration levels within the street, where the

90  application of logarithmic wind profile probably overestimated the bottom wind speed in a deep street canyon as

91  abovementioned. Other models simply assumed that in street canyons, wind direction followed the street direction,

92  and wind speed was uniform, which was not sufficient to resolve the concentration gradient within street canyons

93  (Kim et al., 2018; Benavides et al., 2019). Berchet et al. (2017) proposed a cost-effective method for simulating

94  city-scale pollution taking advantage of high-resolution accurate CFD, while the primary $NO_x$ was predicted due

95  to the lack of a chemical module. Therefore, it is essential to build an integrated model to predict long-term and

96  near-road air pollution suitable for the urban complex underlying surface environment.

97

98  The objective of the present work is to investigate the street-level $NO_2$ concentrations and quantify the contribution

99  of vehicle emissions considering the influence of the refined wind flow in complex urban environment. To this end,

100  a hybrid model CMAQ-RLINE_URBAN was developed by offline coupling the local RLINE model with the

101  regional CMAQ model and some localized urban thermodynamic parameter schemes. Specifically, in order to

102  predict the effects of urban street canyons on the diffusion of pollutants, we developed a Machine Learning-based

103  Street Canyon Flow (MLSCF) parameterization scheme to estimate the wind filed in a cost-effective way, which

104  was based on integrating two machine learning methods using big wind profile data from 1600 CFD simulations.

105  To evaluate the performance of CMAQ-RLINE_URBAN, simulations under several scenarios were conducted in

106  Beijing urban areas from August 1st to 31th of 2019, and validated through comparison with observations from

107  monitoring sites. Furthermore, spatial distribution characteristics of $NO_2$ concentrations in the near-road

108  environment were also analysed in this study.

109

110  **2 Materials and Methods**

111  **2.1 Hybrid model framework**

112  Here, we established the MLSCF scheme based on R language, and modified the code of RLINE model to add

113  other parameterization schemes with FORTRAN language. Finally, a multiscale air quality hybrid model was

114  developed to achieve a high-resolution $NO_2$ pollution mapping in urban areas. The framework of CMAQ-

115  RLINE_URBAN is shown in Figure 1. The hybrid model was established based on RLINE model, offline coupling

116  with the gridded meteorological field provided by WRF model and the pollutant background concentrations from

117  non-vehicle sources provided by CMAQ model with the Integrated Source Apportionment Method (ISAM),

118  considering the thermodynamic effects caused by the complex underlying surface compositions of the city. In our

5

119 hybrid model, a $NO_2$ pollution map with a high temporal (1 h) and spatial resolution (50 m×50 m) can finally be
120 obtained.

121

122 RLINE is a Gaussian line source dispersion model developed by Snyder et al. (2013) to predict pollutant
123 concentrations in near-road environments. In the RLINE model, the mobile source is considered as a finite line
124 source, from which the concentration is found by approximating the line as a series of point sources and integrating
125 the contributions of point sources using an efficient numerical integration scheme. The number of points needed
126 for convergence to the proper solution is a function of distance from the source line to the receptor, and each point
127 source is simulated using a Gaussian plume formulation. The RLINE model performs generally comparable results
128 when evaluated with other line source models for on-road traffic emissions dispersion (Snyder et al., 2013; Heist
129 et al., 2013; Chang et al., 2015), and has been successfully used in many studies to evaluate the impacts from traffic
130 emissions on air quality (Zhai et al., 2016; Valencia et al., 2018; Benavides et al., 2019; Filigrana et al., 2020;
131 Zhang et al., 2021a).

132

133 The simulation for local meteorological conditions in CMAQ-RLINE_URBAN included three steps: Estimation
134 for areas above the top of Urban Canopy Layer (UCL), inside of UCL, and inside of the street canyon. (1) In this
135 study, the configuration of WRF model referred to our previous study (Lv et al., 2020). The height of midpoint in
136 the bottom layer to the ground was set as 22.5 m, which was close to the average height of buildings near street
137 canyons, similar to the settings in the previous study (Benavides et al., 2019). Therefore, the meteorological field
138 simulated by the WRF model was used as the wind field and atmospheric stability at the top of UCL. During the
139 hybrid model running, the meteorological conditions over buildings near each road were obtained separately from
140 WRF model according to the road location. (2) Then, the surface roughness length ($z_0$) of each road was estimated
141 based on the surrounding building geometry and used to recalculate the localized meteorological parameters (e.g.
142 Monin-Obukhov length) within UCL according to the algorithm proposed by Benavides et al. (2019) ($z_0$ scheme).
143 The atmospheric turbulence intensity in urban areas around sunset in the afternoon was obviously enhanced
144 considering the influence of the urban heat island effect based on methods in the AERMOD model (Cimorelli et
145 al., 2005) (UHI scheme). The UHI scheme would affect the turbulent intensity based on the evaluation for the
146 upward surface heat flux and the urban boundary layer height due to convective effects, and then the mixing height,
147 convective velocity scale, surface friction velocity, and Monin-Obhukov length were all recalculated (details in the
148 Supplement Section S1). (3) Finally, the wind field within UCL was calculated according to different types of road
149 environments: open terrain and street canyon. The logarithmic wind profile based on Monin-Obhukov Similarity

150  Theory (MOST) (Foken, 2006) in the original RLINE model was still used when the grid receptor was located in

151  the open terrain (MOST scheme), while the MLSCF parameterization scheme was used for grid receptors within

152  the street canyon to quantitatively characterize the influence of the street canyon geometry and the external wind

153  environment at the top of the roof. The detailed introduction for street canyon geometry and the MLSCF scheme

154  was described in the following section.

155

156  The real-time vehicle emission inventory used in both regional and local air quality models was based on Street-

157  Level On-road Vehicle Emission (SLOVE) Model developed in our previous study (Lv et al., 2020), which was

158  based on the real-time traffic condition data from AMap. The daily averaged $NO_x$ emission from on-road vehicles

159  in Beijing in 2019 was estimated to be 136.0 Mg, of which emissions from heavy duty vehicles and heavy duty

160  trucks accounted for 31% and 34%, respectively. In our simulation, the concentrations of NO, $NO_2$, and $O_3$

161  excluding contributions from vehicle emissions were used as background concentrations at the roof level, avoiding

162  the double counting in the coupling process. These background concentrations were simulated by CMAQ-ISAM

163  model, in which the emissions were divided into local mobile and other four emission groups to trace their

164  contributions separately, so the influence of non-local vehicle emissions was considered, and details were presented

165  in our previous study (Lv et al., 2020). The spatial resolution of the innermost domain in both WRF and CMAQ

166  model was 1.33 km×1.33 km. In addition, the influence of atmospheric turbulence and building geometry on the

167  vertical mixing of background concentration was considered (vertical mixing scheme). The ratios of wind speed at

168  surface and roof levels were used as a proxy to calculate the contribution of background concentration over street

169  canyons to the near-ground level (Benavides et al., 2019). In this scheme, the surface wind was from MLSCF

170  scheme when the gird receptor is located within the street canyon, and otherwise the logarithmic wind profile was

171  used to calculate the wind speed at the specified height, and details were showed in the Supplement Section S2.

172  Finally, combined with the vehicle-induced primary $NO_x$ concentration calculated by the RLINE kernel, the high

173  spatial resolution $NO_2$ map could be simulated considering the photochemical process of $NO_x$. In this study, a

174  simplified two-reaction scheme, including the photolysis of $NO_2$ and the oxidation of NO, was incorporated into

175  the model to characterize the photochemical process of $NO_x$ (details in the Supplement Section S3), which has been

176  successfully applied in the SIRANE dispersion model (Soulhac et al., 2017).

177

178  **2.2 Development for MLSCF scheme**

179  **2.2.1 The database of street canyon geometry**

180  We first established a database of street canyon geometry for 15,398 roads in urban areas of Beijing based on the

181 three-dimensional building data obtained from our previous study (Lv et al., 2020) using Geographic Information

182 System (GIS). Three typical parameters to represent street canyon geometry were investigated, including height

183 ratio ($H_l/H_r$) ($H_l$ is the building height on the left side, while $H_r$ is the building height on the right side), aspect

184 ratio ($H/W$) ($H$ is set to be the average height, and W is the width of the street canyon), the canyon length to height

185 ratio ($L/H$) ($L$ is set to be the length of the street canyon). In this study, the extremely special geometry of canyons

186 was not considered, and the typical street canyons were selected as the following conditions: (1) The proportion of

187 actual street canyon length (the length of road where the buildings nearby) was greater than 0.5; (2) $H/W$ was

188 greater than 0.2; (3) $H_l/H_r$ was between 0.3 and 3.3. Finally, the total number of the typical street canyon was

189 1,889, with a total length of 787 km. The spatial distributions of canyon geometry are shown in Figure S1 in the

190 Supplement. In urban areas of Beijing, street canyon was generally wide with the averaged width of 50.3 m, and

191 buildings on both sides were relatively low with a mean of 23.6 m. Most street canyons were obviously located in

192 areas within the fourth ring road. The shallow ($H/W \leq 0.5$) canyons and long canyons ($L/H > 7$) were dominated,

193 accounting for 54% and 84% of the total number of street canyons.

194

195 **2.2.2 Description of CFD cases**

196 Here, to predict air flow in street canyons comprehensively, CFD simulations were conducted under combinations

197 of different values of controlling factors based on ANSYS FLUENT (v19.2). The controlling factors included the

198 aforementioned three typical parameters to represent canyon geometry, the background wind speed at the height of

199 $H$ ($V(H)$) and the angle between wind direction and street axis (α) to describe the external wind environment. The

200 selected values of each factor were listed in Table 1, and total 1600 (i.e., 5×4×4×5×4) simulations were

201 implemented.

202

203 In this study, the computational domain of three-dimensional (3D) full-scale CFD simulations is shown in Figure

204 2. The average building height $H$ of the street canyon was always set to 21 m in different simulations, which was

205 similar to the mean street canyon height in Beijing. Other actual size of street canyons (e.g., street canyon width

206 $W$) was calculated according to the ratio of each specific simulation. Distances between urban canopy layers (UCL)

207 boundaries and the domain top, domain inlet and domain outlet were set as $5H$, $5H$, and $20H$, respectively.

208

209 The turbulence closure schemes for CFD include the Reynolds-Averaged Navier-Stokes (RANS) and the Large-

210 Eddy Simulation (LES), and the choice of them depends on the computational cost, the accuracy required and the

211 purpose of application. The RANS resolves the mean time-averaged properties with all the turbulence motions to
212 be modelled, while LES adopts a spatial filtering operation and consequently resolves large-scale eddies directly
213 and parameterizes small-scale eddies (Zhong et al., 2016). Compared with the LES, the RANS is more easily
214 established and computationally faster (Xie and Castro, 2006). However, the LES can provide a better prediction
215 of air flow than that from the RANS when handling complex geometries (Dejoan et al., 2010; Santiago et al., 2010).
216 In this study, considering the huge computational burden of a large number of simulations and the relatively simple
217 geometry of street canyons in our modelling, the RANS was selected to characterize the air flow.

218

219 Following the CFD guideline (Tominaga et al., 2008; Franke et al., 2011), zero normal gradient conditions or
220 pressure outlet conditions were applied at the domain outlet, and symmetry boundary conditions were adopted at
221 the domain top and two lateral domain boundaries. For near-wall treatment, no-slip wall boundary conditions with
222 standard wall functions were used (Fluent, 2006). All governing equations for the flow and turbulent quantities
223 were discretized by the finite volume method with the second-order upwind scheme. The SIMPLE scheme was
224 used for the pressure and velocity coupling. The residual for continuity equation, velocity components, turbulent
225 kinetic energy, and its dissipation rate were all below $10^{-5}$. Meanwhile, the CFD simulation would also stop when
226 the iteration steps exceeded 10,000, due to the large computing cost of so many simulations. In summary, the
227 average iteration steps of total 1600 cases were 4,443. About 54.6% of cases met the convergence criteria, and the
228 median residual values of continuity equation, velocity in X axis, velocity in Y axis, velocity in Z axis, $k$ and $\varepsilon$ were
229 $1.0\times10^{-5}$, $8.5\times10^{-7}$, $8.5\times10^{-7}$, $4.1\times10^{-7}$, $3.4\times10^{-6}$ and $5.4\times10^{-6}$, respectively, indicating the overall model
230 performance was acceptable. The selected turbulence model and grid arrangement are discussed in the following
231 section.

232

233 At the domain inlet, the power-law velocity profile (Brown et al., 2001), vertical profiles of turbulent kinetic energy
234 $k_{in}$ and its dissipation rate $\varepsilon_{in}$ at the domain inlet (Lien and Yee, 2004; Zhang et al., 2019a), were described below:

$$U_0(z) = U_{ref}\left(\frac{z}{H_{ref}}\right)^{\alpha}$$

$$k_{in}(z) = \left(I_{in} \times U_0(z)\right)^2$$

$$\varepsilon_{in}(z) = \frac{C_\mu^{3/4} k_{in}^{3/2}}{\kappa z}$$

238   Here, $U_0(z)$ stood for the stream-wise velocity at the height $z$. $U_{ref}$ represented the reference speed. The reference

239   height $H_{ref}$ was 21m. The power-law exponent of $\alpha=0.22$ denoted underlying surface roughness above medium-

240   dense urban area (Kikumoto et al., 2017). Turbulence intensity $I_{in}$ was 0.1, Von Karman constant $\kappa$ was 0.41 and

241   $C_\mu$ was 0.09.

242

243   **2.2.3 The CFD validation**

244   In this study, the stream-wise and vertical velocity predicted by CFD within street canyons was compared with

245   wind tunnel data in previous researches. For buildings of the cube arrays model, wind tunnel data from Brown et

246   al. (2001) was used to evaluate the reliability of CFD results by measuring vertical profiles of velocity. In this

247   experiment, street canyon was perpendicular to the wind direction at the roof level. For long-street models, we

248   predicted horizontal profiles of velocity along the street centerline at the height of z=0.11H or vertical profiles at

249   some points and then validated CFD simulations using wind tunnel data from Hang et al. (2010). In this validation

250   case, the wind direction at the roof level was parallel to the axis of street canyons. The description and validation

251   results are shown in Figure S2-S3, and Table S1 in the Supplement, respectively.

252

253   We identified the influence of different minimum sizes of hexahedral cells near wall surfaces (fine: 0.1m, medium:

254   0.2m, and coarse: 0.5m) and turbulence models (standard k-ε model and RNG k-ε model) on the predicted velocity,

255   to evaluate the grid independence and turbulence model accuracy (Figure S3 in the Supplement). The results

256   indicated that the predictions from the standard k-ε model could well match the variations of observed velocity

257   within the street canyon, of which performances were much better than that of the RNG model. In addition, different

258   grid resolutions used in simulations would not obviously affect the predicted results. We finally adopted the

259   standard k-ε model to characterize turbulence, and the minimum size of hexahedral cells near wall surfaces was

260   0.5 m with an expansion ratio of 1.1 was applied to save the computing cost, and the average mesh number in total

261   80 street canyon models is 1,367,965.

262

263   Moreover, the averaged wind speed from CFD in street canyons with different aspect ratios and external wind

264   direction was compared with predictions from other empirical methods used in SIRANE model (Soulhac et al.,

265   2012) and MUNICH model (Kim et al., 2018). Similar predictions using different methods also proved the

266   reliability of CFD simulation in this study (Figure S4 in the Supplement).

267

### 2.2.4 Machine learning

Data driven method, such as machine learning and deep learning, is now a successful operational geoscientific processing schemes and has co-evolved with data availability over the past decade (Reichstein et al., 2019). Specially, these models have been used as computationally efficient emulators of explicit mechanism models, to explore uncertainties (Aleksankina et al., 2019) and sensitivities or replace complex gas-phase chemistry schemes (Keller and Evans, 2019; Conibear et al., 2021). In addition, meta-models (Fang et al., 2005) such as neural networks and Gaussian process (Beddows et al., 2017) are also used to produce a quick to run model surrogate and show reliable performance. Random Forest (RF) model algorithm is an ensemble learning method that generates many decision trees and aggregates their results, which has been developed to solve the high variance errors typical of a single decision tree (Breiman, 2001). Multivariate Adaptive Regression Splines (MARS) is a nonparametric and nonlinear regression method, which can be regarded as an extension of the multivariate linear model (Friedman, 1991). RF and MARS are common machine learning methods which run efficiently on large data sets, and are relatively robust to outliers and noise. Furthermore, they never require the specification of underlying data model and the complex parameter tuning, and they can still provide efficient alternatives and generally show a high accuracy in applications for predict air pollutant concentrations (Hu et al., 2017; Chen et al., 2018; Kamińska, 2019; Geng et al., 2020).

Here, based on the database including 42,880 samples obtained from 1600 CFD simulations, the RF and MARS were both used to simulate the wind vector along X-axis ($V_x$) and Y-axis ($V_y$) at different heights within the street canyon respectively. The $V_x$ and $V_y$ were the average of all velocities along X or Y axis over the same horizontal profile at a specific height within the street canyons. The input predictor variables included $H/W$, $L/W$, $H_l/H_r$, the grid receptor relative height ($z/H$), the background wind vector at the height of H along X-axis ($Vbg_x = V(H) \times \sin \alpha$) and Y-axis ($Vbg_y = V(H) \times \cos \alpha$). We finally combined the advantages of these two machine learning models and developed the MLSCF scheme to predict wind environment in street canyons and incorporated into the hybrid model, which is discussed in the section 3.1.

In RF model, the number of predictors randomly sampled at each split node in the decision tree ($m_{try}$) and the number of trees to grow ($NumTrees$) are two important hyperparameters that determine the performance of the model. Similarly, in MARS model, the two important hyperparameters are the total number of terms ($nprune$) and the maximum number of interactions ($degree$). By comparing the mean squared error (MSE) for testing datasets

across models with candidate parameter combinations, we set $m_{try}$ and $NumTrees$ as 6 and 200 in RF, respectively, and $nprune$ and $degree$ as 23 and 3 in MARS, respectively. Additionally, the 10-fold cross-validation (CV) repeated ten times were considered to evaluate the prediction performance of our models. The total dataset was randomly divided into 10 subsets, where 9 subsets was used to train model and another was applied for validation. The fitted coefficients of MARS are shown in Table S2-S3 in the Supplement.

In order to identify the sensitivity and response relationship between prediction variables and results in RF model, we used the MSE for out-of-bag (OOB) to evaluate the relative importance of each feature to $V_x$ and $V_y$, by randomly replacing the value of a single prediction variable one by one (Liaw, 2002). Higher values of increase in MSE indicated that the predictor was more important. In addition, Partial Dependence Plots (PDPs) was applied to establish the response relationship between the change of a single predictive variable and the predicted results, considering the average influence of other variables (Greenwell, 2017).

**2.3 Configuration of CMAQ-RLINE_URBAN**

The near-ground $NO_2$ concentrations were simulated from August 1st to 31th in 2019 when the average of daily high temperatures was higher than 30 ℃ and sunlight duration was longer than 13 hours, leading to strong photochemical reactions. The simulation domain for the hybrid model covered the core urban areas within and surrounding the fifth ring road, shown in Figure 3. The receptors included both grid receptors and monitor receptors. The grid receptors were set at a spatial resolution of 50 m×50 m, and the height above the ground was 1.5 m, which was equivalent to the height of the human breathing. We used data from 10 observation stations (monitor receptors) located in the normal urban environment and 5 near-road monitoring sites for validation (Beijing Ecological Environment Monitoring Center, available at http://zx.bjmemc.com.cn/) (DSH, NSH, QM, XZM, and YDM) in the simulation domain (Figure 3), which were 10 meters and 3 meters above the ground respectively. The QM and XZM sites were located in shallow street canyons, and details for the morphometric of near-road measurement sites were shown in Table S4 in the Supplement.

In general, compared to the RLINE model, CMAQ-RLINE_URBAN has the following improvements:

(a) The gridded meteorological parameters provided by the WRF model were used.

(b) Gridded non-vehicle-related concentrations provided by CMAQ-ISAM model were used as background concentrations.

12

328  (c)  A simple $NO_x$ photochemical scheme was incorporated to simulate $NO_2$ concentrations.

329  (d)  Thermodynamic effects caused by the special underlying surface structures of the city were considered,

330  including UHI effects, the influence of local buildings on turbulence intensity and vertical mixing of

331  background concentrations.

332  (e)  A newly developed MLSCF scheme was applied to predict wind environment in street canyons.

333

334  In our simulation, the model configurations in the base scenario CMAQ-RLINE_URBAN included all (a)-(e)

335  schemes, and the other two control scenarios were set to investigate the sensitivity of urban schemes on predictions,

336  where all input data was set to be the same. The scenario CMAQ-RLINE only including (a)-(c) schemes was set to

337  analyze the impacts of urban thermodynamic schemes, and the scenario CMAQ-RLINE_URBAN_nc including

338  (a)-(d) schemes was set to identify the impacts of the MLSCF scheme. Although the wind environment for each

339  road at the top of the canyon was provide by the WRF model in all scenarios, the calculation of wind profile within

340  the street canyon was different. It was estimated based on the MOST theory in the CMAQ-RLINE and CMAQ-

341  RLINE_URBAN_nc rather than that from the MLSCF in the CMAQ-RLINE_URBAN.

342

343  **3 Results**

344  **3.1 Fitting results of machine learning**

345  In this study, the 10-fold cross-validation (CV) repeated ten times was considered to evaluate the prediction

346  performances of RF and MARS models. As shown in Figure 4 and Figure S5, both models performed acceptable

347  robustness in CV, indicating that neither RF nor MARS model overfitted the data. In general, the performances of

348  both models in predicting $V_y$ was better than that in $V_x$ of which the absolute value was relatively small, especially

349  for MARS model. Since $V_x$ was responsible for the formation of the vortex within street canyons and affected by

350  multiple factors, it was more difficult to be simulated. The averages of mean absolute error (MAE), root mean

351  square error (RMSE), and correlation coefficient (R) in the CV of the RF model for $V_x$ and $V_y$ were 0.04 m/s and

352  0.05 m/s, 0.02 m/s and 0.03 m/s, and 0.99, respectively. Although the average of the relative error (RE) was a little

353  high (42.5% and 43%), particularly when the predicted wind speed was low, the median RE were relatively low

354  with 9.8% and 2.7%, respectively, indicating an acceptable performance. Compared with the advanced non-linear

355  RF algorithm, the MARS model performed not very well, especially when the absolute value of $V_x$ was greater than

356  1 m/s and $V_y$ was less than 3 m/s. However, when the predicted wind speed by machine learning methods was

357  compared with observations from wind tunnel experiments, we found that the performance of the MARS model

358 was obviously better than that of RF model in one of validation cases (see Figure 5). The decision tree model like

359 RF failed to respond to the parts beyond the range of prediction variables ($Vbg_y$=17 m/s >>5 m/s), while the more

360 reasonable predictions can be obtained by the MARS model which used piecewise linear function essentially.

361 Therefore, the MLSCF scheme was established based on a method to combine the advantages of each model. The

362 RF model was used when the input value was within the range of predictors shown in Table 1, otherwise the

363 predictions from the MARS model were used.

364

365 In addition, the importance of each predictor variable in the RF model was investigated to explain their impacts on

366 predictions. As shown in Figure 6, the background wind speeds on x and y axis played vital roles in predictions of

367 $V_x$ and $V_y$, respectively, followed by the relative height ($z/H$). Among the geometric parameters of the street

368 canyon, the impact of $L/W$ was least. Since $V_x$ was the main driving force for the formation of vortices in street

369 canyons, it was more affected by the geometry of street canyons especially $H_l/H_r$, comparing to $V_y$. This feature

370 importance ranking was basically consistent with the conclusion in a previous study (Fu et al., 2017). Figure S6 in

371 the Supplement shows the PDPs of each predictor variable in RF model for $V_x$ and $V_y$. As $z/H$ grew, $V_x$ and $V_y$

372 showed linear and logarithmic increase patterns, respectively. And the resistant effect of windward buildings on

373 wind speed enhanced with the increasing of $H_l/H_r$, resulting in a significant decrease in $V_x$ particularly when

374 $H_l/H_r$ was lower than 1.25. The relationship between predictors and results in the model was consistent with the

375 actual mechanism, indicating our model could provide an accurate description of the wind field in the street canyon.

376

377 **3.2 Impacts of MLSCF on simulations in street canyons**

378 We compared the differences between monthly mean wind profile in different street canyons including QM

379 (shallow canyon: $H/W = 0.22$), XZM (shallow canyon: $H/W = 0.35$), SZJ (standard canyon: $H/W = 1$) and

380 JTDL (deep canyon: $H/W = 1.93$), calculated by the default logarithmic function based on MOST in the original

381 RLINE model (Foken, 2006), and the MLSCF scheme developed in this study. As shown in Figure 7(a)-(d), the

382 wind profile estimated by MOST showed a logarithmic change at the height above displacement height ($d_h$) with

383 a decrease to 0 at $d_h$, and remained constant below $d_h$ (the $d_h$ is calculated by multiplying surface roughness length

384 ($z_0$) times a factor which is recommended to be set as 5). Compared with the MOST, the simulated wind speeds

385 near the ground and at the top of canyons were generally lower based on the MLSCF scheme in shallow and

386 standard street canyons. In the deep street canyon, the significant reduction in ventilation volume led to the mean

387 wind speed simulated by the MLSCF scheme much lower than that of MOST at all heights. Although the aspect

388  ratios of the street canyon located in QM and XZM were similar, their orientations were quite different, resulting

389  in significant differences under prevailing external winds in different directions. Since the prevailing northerly and

390  southerly wind was observed in Beijing during the study period, the resistance effect of the buildings on both sides

391  of the east-west street canyon located in QM was more obvious.

392

393  We also investigated the impacts of the MLSCF on hourly wind direction at the bottom ($z = 3m$) of different street

394  canyons by comparing the roof-level predictions from WRF model (see Figure 7(e)-(f)). In the shallow street

395  canyon like QM, the simulated wind direction at the bottom was consistent with the background on the whole, with

396  the R reaching 0.8. When the background wind direction was less than 180°, the averaged wind direction at the

397  bottom simulated by MLSCF was 91.8°, which was basically consistent with the angle between the street and the

398  south direction (84.5°). When the background wind direction was greater than 180°, the average wind direction

399  predicted by MLSCF (257.4°) was similar to that in the opposite direction of the street (264.5°), which was in line

400  with the theory proposed by Soulhac et al. (2008) that the average wind direction in street canyons was assumed to

401  be consistent with the (opposite) orientation of the street. While in the deep street canyon of SZJ, when the external

402  wind perpendicularly blew to the street, the wind direction at the bottom was completely opposite to that at the top

403  due to the formation of vortex, with the R reaching -0.97. In conclusion, compared with the traditional MOST

404  method, the newly developed MLSCF scheme could well simulate the influence of the external wind environment

405  and geometry on the wind field inside the street canyon.

406

407  As shown in Figure 8, the impacts of the MLSCF scheme on simulated $NO_2$ concentration were identified by the

408  differences between CMAQ-RLINE_URBAN and CMAQ-RLINE_URBAN_nc scenario during a clean day

409  (August 24th). When the atmosphere was stable at night, in street canyons with a large aspect ratio, the wind

410  direction at the bottom changed to the opposite to that at the top, combined with the decreased wind speed affected

411  by the MLSCF scheme, the $NO_2$ concentrations at upwind grid receptors increased by up to 80 μg/m³. Meanwhile,

412  the changes in wind direction would also decrease the concentrations at downwind grid receptors by up to 20 μg/m³.

413  For example, in the SZJ standard canyon, the background wind direction over the street was 79° (easterly), and

414  the wind direction at the bottom changed to 291° affected by the MLSCF scheme (westerly). Therefore, the upwind

415  $NO_2$ concentrations increased, and the location of peak $NO_2$ concentration shifted to the windward. Since the

416  changes in $NO_2$ concentrations were also influenced by the local on-road emissions, the increase was only up to

417  2.1 μg/m³ in SJZ street, where the traffic flow and vehicle emissions were small at night. However, a little influence

418  was observed during the day in the convective boundary layer. During this period, although the wind direction at

419 the bottom was not changed obviously due to the parallel background wind in SZJ street, the increased surface

420 wind speed was beneficial for the dispersion, resulting in the decreased concentration in grid receptors within both

421 sides of the street canyon. In summary, the MLSCF scheme enabled the characterization of the concentration

422 distribution in street canyons.

423

**3.3 Performance of near-road simulations from different models**

425 The performances in predicting $NO_2$ concentrations at all monitor receptors from different models were first

426 compared, including CMAQ-RLINE_URBAN, CMAQ-RLINE and CMAQ model. The mean bias (MB), RMSE,

427 normalized mean bias (NMB), normalized mean gross error (NMGE), the fraction of predictions within a factor of

428 two (FAC2), Index of agreement (IOA), and $R$ between simulations and observations were all selected as statistical

429 indicators for the evaluation (Table 2). In general, the performance of CMAQ-RLINE_URBAN was the best at all

430 urban sites. Compared to the CMAQ model, the averaged MB and NMB at urban sites in the hybrid model

431 decreased from 8 $\mu g/m^3$ to 1.3 $\mu g/m^3$ and 27% to 4%, respectively.

432

433 Diurnal variations of observed and predicted hourly averaged $NO_2$ concentrations at near-road sites from different

434 models were mainly compared and shown in Figure 9. The comparison of hourly and daily averaged concentrations

435 is shown in Figure 10. Overall, the CMAQ-RLINE_URBAN performed best with the smallest deviations. By

436 comparing the performances of the CMAQ and CMAQ-RLINE scenario, we found the direct coupling between the

437 CMAQ and RLINE models could reproduce the high $NO_2$ concentrations at near-road sites in daytime, and

438 significantly improve the underestimation of near-source concentrations due to grid dilution on emissions in

439 CMAQ model. The averaged MB and NMB at all sites changed from -10 $\mu g/m^3$ to 25.6 $\mu g/m^3$, and from -20% to

440 51%, respectively. However, a significant overestimation was found in the CMAQ-RLINE at night (0:00-6:00) and

441 around sunset in the afternoon (16:00-23:00), of which the peak could exceed the observed concentrations by more

442 than 1 times. This overestimation was reduced in the CMAQ-RLINE_URBAN, where the urban thermodynamic

443 schemes were implemented. The averaged MB and NMB decreased to 6.3 $\mu g/m^3$ and 12%, respectively, due to the

444 following reasons: (1) The increased surface roughness length slightly enhanced local turbulence intensity near

445 roads; (2) The UHI scheme enhanced the intensity of atmospheric turbulence in urban areas before and after sunset

446 in the afternoon; (3) The effect of turbulence intensity on the local vertical mixing of background concentrations

447 was considered, significantly reducing the mixing ratio of concentrations over UCL and near the ground at nights

448 in the stable boundary layer (Figure S7 in the Supplement), which was probably the main driving force of decreased

449 predictions in the hybrid model (Benavides et al., 2019). However, the CMAQ-RLINE_URBAN slightly

16

450  overestimated the nighttime $NO_2$ concentration of all observation stations except the DSH, which was probably

451  caused by overestimations of background concentrations from CMAQ-ISAM and vehicle emissions.

452

453  The accuracy of model performances at each traffic site showed a little difference affected by the variations in the

454  traffic flow and emissions of nearby roads, as well as the geometry of surrounding buildings and street canyons. At

455  DSH and NSH sites, which were adjacent to ring roads as the main urban freight corridors with a high traffic flow

456  including a large proportion of trucks, the high $NO_x$ emissions led to the highest roadside $NO_2$ observations among

457  all sites. The CMAQ model would significantly underestimate the high $NO_2$ concentration at sites nearby ring roads,

458  with MB and NMB lower than -15 $\mu g/m^3$ and -28% (Table S5 in the Supplement), respectively, which was

459  improved using CMAQ-RLINE_URBAN. However, the hybrid model performed a minor overestimation at the

460  NSH site, since the monitor was actually positioned in the road centerline but assumed to be located downwind in

461  the model, resulting in a relatively large systematically error (Snyder et al., 2013). In total, CMAQ-

462  RLINE_URBAN performed best among all models, especially improving the estimation of $NO_2$ concentrations

463  near roads by the original regional model.

464

465  Additionally, Figure S8 in the Supplement shows the comparison between simulated and observed roadside hourly

466  and daily maximum 8-hour average $O_3$ concentrations by different models, and their diurnal variations are shown

467  in Figure S9. Generally, the hybrid model significantly improved the overestimation of daytime $O_3$ concentrations

468  by the CMAQ model when considering the titration effect of high NO concentration near roads on $O_3$. In the hybrid

469  model, the peak time was delayed to about 15:00, which was closer to the observation, but still 1-2 hours earlier

470  than the actual time, which may be related to the uncertainty in $NO_2$ photolysis rate.

471

472  **3.4 Spatial distribution characteristics of simulated concentrations**

473  We investigated the differences between the spatial distribution of the monthly averaged $NO_2$ concentration

474  simulated by the CMAQ and CMAQ-RLINE_URBAN models, as shown in Figure 11. Since the urban

475  thermodynamic schemes were considered in the hybrid model, the overestimation of most urban environmental

476  grid receptors by CMAQ model was relieved. Within the fourth ring road and its surrounding areas, the mean

477  concentration of $NO_2$ from CMAQ-RLINE_URBAN was 30.1 $\mu g/m^3$, lower than that from the CMAQ model (39.5

478  $\mu g/m^3$). The overall spatial distribution characteristics of $NO_2$ predictions from both models showed that the

479  concentrations in south regions were high due to the pollution transport from Hebei province (An et al., 2019).

480  However, near-road hotspots for the $NO_2$ pollution were identified in the hybrid model where the spatial resolution

17

481    of results increased to 50 m×50 m. The $NO_2$ concentrations nearby ring roads with high traffic flow and emissions

482    were up to 120 $\mu g/m^3$, much higher than the maximum prediction from CMAQ model (52.4 $\mu g/m^3$). In addition,

483    the simulated near-road concentrations from the hybrid model during traffic peak hours (18:00-19:00) were

484    significantly higher than those at noon (12:00-13:00), while there were few changes in results from CMAQ model

485    (Figure S10 in the Supplement).

486

487    The $NO_2$ concentrations estimated by CMAQ-RLINE_URBAN at all grid receptors grids followed a two-mode

488    Gaussian distribution (Figure S11 in the Supplement), which was similar to Zhang's results (Zhang et al., 2021b).

489    The $NO_2$ concentrations as a result of vehicle emissions were further calculated by the differences between the total

490    and background concentrations. In general, the vehicle-induced $NO_2$ concentrations in urban areas was 11.8 $\mu g/m^3$,

491    accounting for 39% of the total concentrations, which was similar to the predicted contribution from the CMAQ-

492    ISAM model (42.5%).

493

494    Figure 12 shows the changes in $NO_2$ concentrations simulated by the hybrid model with distance from the grid

495    receptors to its nearest road centerline. The concentrations at grid receptors within 200 m from road were

496    significantly affected by vehicle emissions. Within 50 m around the road, as the distance from grid receptors to the

497    road centerline gradually increased, the $NO_2$ concentrations decreased exponentially. The total $NO_2$ concentrations

498    decreased from 53.1 $\mu g/m^3$ to 30 $\mu g/m^3$, and the vehicle-induced concentrations also dropped from 34.7 $\mu g/m^3$ to

499    12.6 $\mu g/m^3$. The concentrations near roads with different types were highly dependent on the emission intensity.

500    The $NO_2$ concentration was highest in the center of the urban freeway, which was 76 $\mu g/m^3$ and about 1.9 times

501    higher than that on local roads. The relative contribution of vehicle emissions to $NO_2$ concentration reached up to

502    75.3% on urban freeways, as well as 71.9% and 65.5% on artery roads and freeways, but only 51.1% on local roads.

503    It was worth noting that although the $NO_2$ concentrations at far grid receptors to the road on highways were slightly

504    higher than those on other road types, the contribution of vehicle emissions was the least. It was since the $NO_x$

505    emission intensity of freeways was as high as that on artery roads, but the density and height of buildings around

506    freeways were usually low, resulting in a high vertical flux of background concentrations from the top of UCL to

507    the ground. In conclusion, the results from the hybrid model accurately reflected not only the impacts of local on-

508    road emissions, but also the pollution characteristics affected by non-vehicle sources at the regional scale.

509

## 4 Conclusion and Discussions

In this study, we developed a hybrid model CMAQ-RLINE_URBAN to quantitatively analyse the effects of vehicle emissions on urban roadside $NO_2$ concentrations at a high spatial resolution of 50 m × 50 m. The main conclusions of this study are as follows:

The developed MLSCF scheme revealed that affected by the geometry of buildings on both sides of the road, the wind filed in the street canyon sometimes was quite different from that in the environmental background. In deep street canyons, the wind speed at the bottom decreased obviously due to the resistant effect of buildings, and the directions of horizontal flow at bottom and top of the canyon were completely opposite due to the formation of vortex. The application of MLSCF scheme in the hybrid model led to increase $NO_2$ concentrations at upwind grid receptors within deep street canyons due to changes in the wind environment. However, the influence of the turbulence induced by street canyon effects on the mixing of air pollution was not considered on which we will make effort in the future.

The comparison between observations and predictions showed that the hybrid model significantly improved the underestimation of near-source concentrations due to grid dilution on emissions in CMAQ model. The implementation of the urban thermodynamic schemes in the hybrid model also relieved the overestimation in night-time $NO_2$ concentrations from the CMAQ directly coupled with RLINE model. The predictions from CMAQ-RLINE_URBAN model could accurately reflect not only the impact of road local emissions, but also the pollution characteristics of non-vehicle sources at regional level. It revealed that in summer, the average contribution of vehicle emission to $NO_2$ concentrations in urban areas of Beijing was 11.8 μg/m³, and the relative contribution accounted for approximately 39%. Moreover, the vehicle-induced $NO_2$ pollution increased significantly with the decreased distance to the road centerline, especially reaching 76 μg/m³ (75%) on urban freeways.

On the basis of this study, the following perspectives are proposed for future research: (1) At present, the execution time during 1 h running CMAQ-RLINE_URBAN over the urban domain was about 3.9 hours in average, which reached 4.8 hours at night due to the difficulty of convergence in the condition of the high atmospheric stability. Therefore, considering the running cost, the grid resolution of area in Beijing 5th ring road and its surroundings can reach 50 m×50 m. We will make efforts to develop a parallel computing method to reduce the computing time, in order to improve the grid resolution of a relatively large-scale simulation. (2) In our study, a simplified two-reaction scheme was incorporated into the model to characterize the photochemical process of $NO_x$, since it

541 performed similar predictions and less computational time compared with those of the complicated CB05 gas phase

542 chemical mechanism (Kim et al., 2018). However, another study pointed that the impact of nonlinear $O_3$-$NO_x$-VOC

543 chemistry on $NO_2$ concentrations in the deep canyon was nonnegligible (Zhong et al., 2017). The influence of

544 different chemistry schemes on near-road simulation will be investigated in the future. (3) The long-term site-

545 observation of wind environment and pollutant concentrations in various street canyons were suggested to be

546 compared with modelling results, especially in deep street canyons with large aspect ratio. The navigation

547 monitoring technology would be applied in the model verification, which can carry out large-scale observation of

548 concentration along streets. (4) Here, we considered the dynamic impact of idealized building structure on wind

549 environment in street canyons. However, there are many other influencing factors, such as building layout and

550 arrangement, roof shape, green vegetation, and thermodynamic effect, which are suggested to be considered in

551 future studies. (5) In this study, we mainly focused on the $NO_2$ concentrations. In fact, the concentration of

552 particulate matter, especially UFP, will also have an obvious peak near the road centerline. In the future, the process

553 of physical and chemical changes of particulate matter near the vehicle exhaust outlet should be further investigated.

554 (6) The high resolution $NO_2$ concentration map was benefit for the estimation of human health risks induced by the

555 air pollution at the street level in future researches.

556

## Data availability

558 Data are available upon request from the corresponding author Huan Liu (liu_env@tsinghua.edu.cn).

559

## Code availability

561 The RF and MARS model for MLSCF are both available on Github (https://github.com/claus0224/MLSCF-RF-

562 MARS), and other codes are available from the corresponding author on reasonable request.

563

570

## Author contributions

Z. Lv and Z. Luo contributed equally. Z. Lv and Z. Luo designed the research and wrote the manuscript. H.L., Y.Z. and K.H. provided guidance on the research and revised the paper. Z. Lv, Z. Luo, and F.D. provided multiple analytical perspective on this research. X.W., J.Z., and L.X. helped collect and clean the data. T.H. helped on language modification.

## Competing interests

The authors declare that they have no conflict of interest.

## Additional information

The supplement is available for this paper at online resources.

Correspondence and requests for materials should be addressed to H.L.

## References

Aleksankina, K., Reis, S., Vieno, M., and Heal, M. R.: Advanced methods for uncertainty assessment and global sensitivity analysis of an Eulerian atmospheric chemistry transport model, Atmospheric Chemistry and Physics, 19, 2881-2898, 2019.

An, Z., Huang, R.-J., Zhang, R., Tie, X., Li, G., Cao, J., Zhou, W., Shi, Z., Han, Y., Gu, Z., and Ji, Y.: Severe haze in northern China: A synergy of anthropogenic emissions and atmospheric processes, Proceedings of the National Academy of Sciences of the United States of America, 116, 8657-8666, 10.1073/pnas.1900125116, 2019.

Beddows, A. V., Kitwiroon, N., Williams, M. L., and Beevers, S. D.: Emulation and Sensitivity Analysis of the Community Multiscale Air Quality Model for a UK Ozone Pollution Episode, Environmental Science & Technology, 51, 6229-6236, 10.1021/acs.est.6b05873, 2017.

Benavides, J., Snyder, M., Guevara, M., Soret, A., Pérez García-Pando, C., Amato, F., Querol, X., and Jorba, O.: CALIOPE-Urban v1.0: coupling R-LINE with a mesoscale air quality modelling system for urban air quality forecasts over Barcelona city (Spain), Geosci. Model Dev., 12, 2811-2835, 10.5194/gmd-12-2811-2019, 2019.

Berchet, A., Zink, K., Muller, C., Oettl, D., Brunner, J., Emmenegger, L., and Brunner, D.: A cost-effective method for simulating city-wide air flow and pollutant dispersion at building resolving scale, Atmospheric Environment, 158, 181-196, https://doi.org/10.1016/j.atmosenv.2017.03.030, 2017.

Breiman, L.: Random Forests, Machine Learning, 45, 5-32, 10.1023/A:1010933404324, 2001.

Brown, M., Lawson, R., DeCroix, D., and Lee, R.: COMPARISON OF CENTERLINE VELOCITY MEASUREMENTS OBTAINED AROUND 2D AND 3D BUILDING ARRAYS IN A WIND TUNNEL, 2001.

Byun, D. and Schere, K. L.: Review of the Governing Equations, Computational Algorithms, and Other Components of the Models-3 Community Multiscale Air Quality (CMAQ) Modeling System, Applied Mechanics Reviews, 59, 51-77, 10.1115/1.2128636, 2006.

Chang, S. Y., Vizuete, W., Valencia, A., Naess, B., Isakov, V., Palma, T., Breen, M., and Arunachalam, S.: A modeling framework for characterizing near-road air pollutant concentration at community scales, Science of the Total Environment, 538, 905-921, 2015.

Chen, G., Li, S., Knibbs, L. D., Hamm, N. A., Cao, W., Li, T., Guo, J., Ren, H., Abramson, M. J., and Guo, Y.: A machine learning method to estimate PM2. 5 concentrations across China with remote sensing, meteorological and land use information, Science of the Total Environment, 636, 52-60, 2018.

Cheng, J., Su, J., Cui, T., Li, X., Dong, X., Sun, F., Yang, Y., Tong, D., Zheng, Y., Li, Y., Li, J., Zhang, Q., and He, K.: Dominant role of emission reduction in PM2.5 air quality improvement in Beijing during 2013–2017: a model-based decomposition analysis, Atmos. Chem. Phys., 19, 6125-6146, 10.5194/acp-19-6125-2019, 2019.

Cimorelli, A. J., Perry, S. G., Venkatram, A., Weil, J. C., Paine, R. J., Wilson, R. B., Lee, R. F., Peters, W. D., and Brode, R. W.: AERMOD: A Dispersion Model for Industrial Source Applications. Part I: General Model Formulation and Boundary Layer Characterization, Journal of Applied Meteorology, 44, 682-693, 10.1175/JAM2227.1, 2005.

Conibear, L., Reddington, C. L., Silver, B. J., Chen, Y., Knote, C., Arnold, S. R., and Spracklen, D. V.: Statistical Emulation of Winter Ambient Fine Particulate Matter Concentrations From Emission Changes in China, GeoHealth, 5, e2021GH000391, https://doi.org/10.1029/2021GH000391, 2021.

Cui, Y., Wang, L., Jiang, L., Liu, M., Wang, J., Shi, K., and Duan, X.: Dynamic spatial analysis of NO2 pollution over China: Satellite observations and spatial convergence models, Atmospheric Pollution Research, 12, 89-99, https://doi.org/10.1016/j.apr.2021.02.003, 2021.

Dejoan, A., Santiago, J., Martilli, A., Martin, F., and Pinelli, A.: Comparison between large-eddy simulation and Reynolds-averaged Navier–Stokes computations for the MUST field experiment. Part II: effects of incident wind angle deviation on the mean flow and plume dispersion, Boundary-layer meteorology, 135, 133-150, 2010.

Fang, K.-T., Li, R., and Sudjianto, A.: Design and modeling for computer experiments, Chapman and Hall/CRC2005.

Filigrana, P., Milando, C., Batterman, S., Levy, J. I., Mukherjee, B., and Adar, S. D.: Spatiotemporal variations in traffic activity and their influence on air pollution levels in communities near highways, Atmospheric Environment, 242, 117758, https://doi.org/10.1016/j.atmosenv.2020.117758, 2020.

FLUENT: FLUENT V6.3. User's Manual. Available online: http://www.fluent.com (accessed on 20 August 2017). 2006.

Foken, T.: 50 Years of the Monin–Obukhov Similarity Theory, Boundary-Layer Meteorology, 119, 431-447, 10.1007/s10546-006-9048-6, 2006.

Franke, J., Hellsten, A., Schlunzen, K. H., and Carissimo, B.: The COST 732 Best Practice Guideline for CFD simulation of flows in the urban environment: a summary, International Journal of Environment and Pollution, 44, 419-427, 10.1504/IJEP.2011.038443, 2011.

Friedman, J. H.: Multivariate adaptive regression splines, The annals of statistics, 19, 1-67, 1991.

Fu, X., Liu, J., Ban-Weiss, G. A., Zhang, J., Huang, X., Ouyang, B., Popoola, O., and Tao, S.: Effects of canyon geometry on the distribution of traffic-related air pollution in a large urban area: Implications of a multi-canyon air pollution dispersion model, Atmospheric Environment, 165, 111-121, https://doi.org/10.1016/j.atmosenv.2017.06.031, 2017.

Geng, G., Meng, X., He, K., and Liu, Y.: Random forest models for PM2. 5 speciation concentrations using MISR fractional AODs, Environmental Research Letters, 15, 034056, 2020.

Grell, G. A., Peckham, S. E., Schmitz, R., McKeen, S. A., Frost, G., Skamarock, W. C., and Eder, B.: Fully coupled "online" chemistry within the WRF model, Atmospheric Environment, 39, 6957-6975, https://doi.org/10.1016/j.atmosenv.2005.04.027, 2005.

Hagler, G. S. W., Thoma, E. D., and Baldauf, R. W.: High-Resolution Mobile Monitoring of Carbon Monoxide and Ultrafine Particle Concentrations in a Near-Road Environment, Journal of the Air & Waste Management Association, 60, 328-336, 10.3155/1047-3289.60.3.328, 2012.

Hang, J., Sandberg, M., Li, Y., and Claesson, L.: Flow mechanisms and flow capacity in idealized long-street city models, Building and Environment, 45, 1042-1053, https://doi.org/10.1016/j.buildenv.2009.10.014, 2010.

He, J., Wu, L., Mao, H., Liu, H., Jing, B., Yu, Y., Ren, P., Feng, C., and Liu, X.: Development of a vehicle emission inventory with high temporal–spatial resolution based on NRT traffic data and its impact on air pollution in Beijing – Part 2: Impact of vehicle emission on urban air quality, Atmos. Chem. Phys., 16, 3171-3184, 10.5194/acp-16-3171-2016, 2016.

Heist, D., Isakov, V., Perry, S., Snyder, M., Venkatram, A., Hood, C., Stocker, J., Carruthers, D., Arunachalam, S., and Owen, R. C.: Estimating near-road pollutant dispersion: A model inter-comparison, Transportation Research Part D: Transport and Environment, 25, 93-105, 2013.

Hood, C., MacKenzie, I., Stocker, J., Johnson, K., Carruthers, D., Vieno, M., and Doherty, R.: Air quality simulations for London using a coupled regional-to-local modelling system, Atmos. Chem. Phys., 18, 11221-11245, 10.5194/acp-18-11221-2018, 2018.

Hu, X., Belle, J. H., Meng, X., Wildani, A., Waller, L. A., Strickland, M. J., and Liu, Y.: Estimating PM2. 5 concentrations in the conterminous United States using the random forest approach, Environmental science & technology, 51, 6936-6944, 2017.

Jensen, S. S., Ketzel, M., Becker, T., Christensen, J., Brandt, J., Plejdrup, M., Winther, M., Nielsen, O.-K., Hertel, O., and Ellermann, T.: High resolution multi-scale air quality modelling for all streets in Denmark, Transportation Research Part D: Transport and Environment, 52, 322-339, https://doi.org/10.1016/j.trd.2017.02.019, 2017.

Jin, Y., Andersson, H., and Zhang, S.: Air Pollution Control Policies in China: A Retrospective and Prospects, International Journal of Environmental Research and Public Health, 13, 1219, 2016.

Kakosimos, K. E., Hertel, O., Ketzel, M., and Berkowicz, R.: Operational Street Pollution Model (OSPM) – a review of performed application and validation studies, and future prospects, Environmental Chemistry, 7, 485-503, https://doi.org/10.1071/EN10070, 2010.

Kamińska, J. A.: A random forest partition model for predicting NO2 concentrations from traffic flow and meteorological conditions, Science of the Total Environment, 651, 475-483, 2019.

Ke, W., Zhang, S., Wu, Y., Zhao, B., Wang, S., and Hao, J.: Assessing the Future Vehicle Fleet Electrification: The Impacts on Regional and Urban Air Quality, Environmental Science & Technology, 51, 1007-1016, 10.1021/acs.est.6b04253, 2017.

Keller, C. A. and Evans, M. J.: Application of random forest regression to the calculation of gas-phase chemistry within the GEOS-Chem chemistry model v10, Geoscientific Model Development, 12, 1209-1225, 2019.

Ketzel, M., Jensen, S., Brandt, J., Ellermann, T., Berkowicz, R., and Hertel, O.: Evaluation of the street pollution model OSPM for measurement at 12 street stations using using newly developed and freely available evaluation tool, J. Civil. Environ. Eng., 2012.

Khaniabadi, Y. O., Goudarzi, G., Daryanoosh, S. M., Borgini, A., Tittarelli, A., and De Marco, A.: Exposure to PM10, NO2, and O3 and impacts on human health, Environmental Science and Pollution Research, 24, 2781-2789, 10.1007/s11356-016-8038-6, 2017.

Kheirbek, I., Haney, J., Douglas, S., Ito, K., and Matte, T.: The contribution of motor vehicle emissions to ambient fine particulate matter public health impacts in New York City: a health burden assessment, Environmental Health, 15, 89, 10.1186/s12940-016-0172-6, 2016.

Kikumoto, H., Ooka, R., Sugawara, H., and Lim, J.: Observational study of power-law approximation of wind profiles within an urban boundary layer for various wind conditions, Journal of Wind Engineering and Industrial Aerodynamics, 164, 13-21, https://doi.org/10.1016/j.jweia.2017.02.003, 2017.

Kim, Y., Wu, Y., Seigneur, C., and Roustan, Y.: Multi-scale modeling of urban air pollution: development and application of a Street-in-Grid model (v1.0) by coupling MUNICH (v1.0) and Polair3D (v1.8.1), Geosci. Model Dev., 11, 611-629, 10.5194/gmd-11-611-2018, 2018.

Lefebvre, W., Van Poppel, M., Maiheu, B., Janssen, S., and Dons, E.: Evaluation of the RIO-IFDM-street canyon model chain, Atmospheric Environment, 77, 325-337, https://doi.org/10.1016/j.atmosenv.2013.05.026, 2013.

692 Liaw, A., Wiener, M. : Classification and regression by randomForest, R News, 2, 18–22, 2002.

693 Lien, F.-S. and Yee, E.: Numerical Modelling of the Turbulent Flow Developing Within and Over a 3-D Building Array, Part
694 I: A High-Resolution Reynolds-Averaged Navier—Stokes Approach, Boundary-Layer Meteorology, 112, 427-466,
695 10.1023/B:BOUN.0000030654.15263.35, 2004.

696 Luo, Z., Xu, H., Zhang, Z., Zheng, S., and Liu, H.: Year-round changes in tropospheric nitrogen dioxide caused by COVID-
697 19 in China using satellite observation, Journal of Environmental Sciences, https://doi.org/10.1016/j.jes.2022.01.013, 2022a.

698 Luo, Z., Wang, Y., Lv, Z., He, T., Zhao, J., Wang, Y., Gao, F., Zhang, Z., and Liu, H.: Impacts of vehicle emission on air quality
699 and human health in China, Science of The Total Environment, 813, 152655, https://doi.org/10.1016/j.scitotenv.2021.152655,
700 2022b.

701 Lv, Z., Wang, X., Deng, F., Ying, Q., Archibald, A. T., Jones, R. L., Ding, Y., Cheng, Y., Fu, M., Liu, Y., Man, H., Xue, Z., He,
702 K., Hao, J., and Liu, H.: Source–Receptor Relationship Revealed by the Halted Traffic and Aggravated Haze in Beijing during
703 the COVID-19 Lockdown, Environmental Science & Technology, 54, 15660-15670, 10.1021/acs.est.0c04941, 2020.

704 Greenwell B M.: pdp: An R Package for Constructing Partial Dependence Plots, R Journal, 9(1): 421., 2017.

705 Mallet, V., Tilloy, A., Poulet, D., Girard, S., and Brocheton, F.: Meta-modeling of ADMS-Urban by dimension reduction and
706 emulation, Atmospheric Environment, 184, 37-46, https://doi.org/10.1016/j.atmosenv.2018.04.009, 2018.

707 Manning, A. J., Nicholson, K. J., Middleton, D. R., and Rafferty, S. C.: Field Study of Wind and Traffic to Test a Street Canyon
708 Pollution Model, Environmental Monitoring and Assessment, 60, 283-313, 10.1023/A:1006187301966, 2000.

709 Masey, N., Hamilton, S., and Beverland, I. J.: Development and evaluation of the RapidAir® dispersion model, including the
710 use of geospatial surrogates to represent street canyon effects, Environmental Modelling & Software, 108, 253-263,
711 https://doi.org/10.1016/j.envsoft.2018.05.014, 2018.

712 Mu, Q., Denby, B. R., Wærsted, E. G., and Fagerli, H.: Downscaling of air pollutants in Europe using uEMEP_v6, Geosci.
713 Model Dev., 15, 449-465, 10.5194/gmd-15-449-2022, 2022.

714 Murena, F., Favale, G., Vardoulakis, S., and Solazzo, E.: Modelling dispersion of traffic pollution in a deep street canyon:
715 Application of CFD and operational models, Atmospheric Environment, 43, 2303-2311,
716 https://doi.org/10.1016/j.atmosenv.2009.01.038, 2009.

717 Nayeb Yazdi, M., Delavarrafiee, M., and Arhami, M.: Evaluating near highway air pollutant levels and estimating emission
718 factors: Case study of Tehran, Iran, Science of The Total Environment, 538, 375-384,
719 https://doi.org/10.1016/j.scitotenv.2015.07.141, 2015.

720 Nguyen, C., Soulhac, L., and Salizzoni, P.: Source Apportionment and Data Assimilation in Urban Air Quality Modelling for
721 NO2: The Lyon Case Study, Atmosphere, 9, 10.3390/atmos9010008, 2018.

722 Oke, T. R.: Street design and urban canopy layer climate, Energy and Buildings, 11, 103-113, https://doi.org/10.1016/0378-
723 7788(88)90026-6, 1988.

724 Pandey, J. S., Kumar, R., and Devotta, S.: Health risks of NO2, SPM and SO2 in Delhi (India), Atmospheric Environment, 39,
725 6868-6874, https://doi.org/10.1016/j.atmosenv.2005.08.004, 2005.

726 Patterson, R. F. and Harley, R. A.: Evaluating near-roadway concentrations of diesel-related air pollution using RLINE,
727 Atmospheric Environment, 199, 244-251, https://doi.org/10.1016/j.atmosenv.2018.11.016, 2019.

728 Reichstein, M., Camps-Valls, G., Stevens, B., Jung, M., Denzler, J., Carvalhais, N., and Prabhat: Deep learning and process
729 understanding for data-driven Earth system science, Nature, 566, 195-204, 10.1038/s41586-019-0912-1, 2019.

730 Santiago, J., Dejoan, A., Martilli, A., Martin, F., and Pinelli, A.: Comparison between large-eddy simulation and Reynolds-
731 averaged Navier–Stokes computations for the MUST field experiment. Part I: study of the flow for an incident wind directed
732 perpendicularly to the front array of containers, Boundary-Layer Meteorology, 135, 109-132, 2010.

Shah, V., Jacob, D. J., Li, K., Silvern, R. F., Zhai, S., Liu, M., Lin, J., and Zhang, Q.: Effect of changing NOx lifetime on the seasonality and long-term trends of satellite-observed tropospheric NO2 columns over China, Atmos. Chem. Phys., 20, 1483-1495, 10.5194/acp-20-1483-2020, 2020.

Snyder, M. G., Venkatram, A., Heist, D. K., Perry, S. G., Petersen, W. B., and Isakov, V.: RLINE: A line source dispersion model for near-surface releases, Atmospheric Environment, 77, 748-756, https://doi.org/10.1016/j.atmosenv.2013.05.074, 2013.

Soulhac, L., Perkins, R. J., and Salizzoni, P.: Flow in a Street Canyon for any External Wind Direction, Boundary-Layer Meteorology, 126, 365-388, 10.1007/s10546-007-9238-x, 2008.

Soulhac, L., Nguyen, C., Volta, P., and Salizzoni, P.: The model SIRANE for atmospheric urban pollutant dispersion. PART III: Validation against NO 2 yearly concentration measurements in a large urban agglomeration, Atmospheric Environment, 167, 10.1016/j.atmosenv.2017.08.034, 2017.

Soulhac, L., Salizzoni, P., Mejean, P., Didier, D., and Rios, I.: The model SIRANE for atmospheric urban pollutant dispersion; PART II, validation of the model on a real case study, Atmospheric Environment, 49, 320-337, https://doi.org/10.1016/j.atmosenv.2011.11.031, 2012.

Stocker, J., Hood, C., Carruthers, D., and McHugh, C.: ADMS-Urban: developments in modelling dispersion from the city scale to the local scale, International Journal of Environment and Pollution, 50, 308-316, 10.1504/IJEP.2012.051202, 2012.

Tominaga, Y., Mochida, A., Yoshie, R., Kataoka, H., Nozu, T., Yoshikawa, M., and Shirasawa, T.: AIJ guidelines for practical applications of CFD to pedestrian wind environment around buildings, Journal of Wind Engineering and Industrial Aerodynamics, 96, 1749-1761, https://doi.org/10.1016/j.jweia.2008.02.058, 2008.

Valencia, A., Venkatram, A., Heist, D., Carruthers, D., and Arunachalam, S.: Development and evaluation of the R-LINE model algorithms to account for chemical transformation in the near-road environment, Transportation Research Part D: Transport and Environment, 59, 464-477, 2018.

Vara-Vela, A., Andrade, M. F., Kumar, P., Ynoue, R. Y., and Muñoz, A. G.: Impact of vehicular emissions on the formation of fine particles in the Sao Paulo Metropolitan Area: a numerical study with the WRF-Chem model, Atmos. Chem. Phys., 16, 777-797, 10.5194/acp-16-777-2016, 2016.

Xie, Z. and Castro, I. P.: LES and RANS for turbulent flow over arrays of wall-mounted obstacles, Flow, Turbulence and Combustion, 76, 291-312, 2006.

Yu, M., Zhu, Y., Lin, C.-J., Wang, S., Xing, J., Jang, C., Huang, J., Huang, J., Jin, J., and Yu, L.: Effects of air pollution control measures on air quality improvement in Guangzhou, China, Journal of Environmental Management, 244, 127-137, https://doi.org/10.1016/j.jenvman.2019.05.046, 2019.

Zhai, X., Russell, A. G., Sampath, P., Mulholland, J. A., Kim, B.-U., Kim, Y., and D'Onofrio, D.: Calibrating R-LINE model results with observational data to develop annual mobile source air pollutant fields at fine spatial resolution: Application in Atlanta, Atmospheric Environment, 147, 446-457, 2016.

Zhang, K., Chen, G., Wang, X., Liu, S., Mak, C. M., Fan, Y., and Hang, J.: Numerical evaluations of urban design technique to reduce vehicular personal intake fraction in deep street canyons, Science of The Total Environment, 653, 968-994, https://doi.org/10.1016/j.scitotenv.2018.10.333, 2019a.

Zhang, Q., Tong, P., Liu, M., Lin, H., Yun, X., Zhang, H., Tao, W., Liu, J., Wang, S., Tao, S., and Wang, X.: A WRF-Chem model-based future vehicle emission control policy simulation and assessment for the Beijing-Tianjin-Hebei region, China, Journal of Environmental Management, 253, 109751, https://doi.org/10.1016/j.jenvman.2019.109751, 2020.

Zhang, Q., Zheng, Y., Tong, D., Shao, M., Wang, S., Zhang, Y., Xu, X., Wang, J., He, H., Liu, W., Ding, Y., Lei, Y., Li, J., Wang, Z., Zhang, X., Wang, Y., Cheng, J., Liu, Y., Shi, Q., Yan, L., Geng, G., Hong, C., Li, M., Liu, F., Zheng, B., Cao, J., Ding, A., Gao, J., Fu, Q., Huo, J., Liu, B., Liu, Z., Yang, F., He, K., and Hao, J.: Drivers of improved PM$_{2.5}$ air quality in China from 2013 to 2017, Proceedings of the National Academy of Sciences, 116, 24463-24469,

776     10.1073/pnas.1907956116, 2019b.

777     Zhang, X., Just, A. C., Hsu, H.-H. L., Kloog, I., Woody, M., Mi, Z., Rush, J., Georgopoulos, P., Wright, R. O., and Stroustrup,
778     A.: A hybrid approach to predict daily NO2 concentrations at city block scale, Science of The Total Environment, 761, 143279,
779     https://doi.org/10.1016/j.scitotenv.2020.143279, 2021a.

780     Zhang, Y., Ye, X., Wang, S., He, X., Dong, L., Zhang, N., Wang, H., Wang, Z., Ma, Y., Wang, L., Chi, X., Ding, A., Yao, M.,
781     Li, Y., Li, Q., Zhang, L., and Xiao, Y.: Large-eddy simulation of traffic-related air pollution at a very high resolution in a mega-
782     city: evaluation against mobile sensors and insights for influencing factors, Atmos. Chem. Phys., 21, 2917-2929, 10.5194/acp-
783     21-2917-2021, 2021b.

784     Zheng, B., Tong, D., Li, M., Liu, F., Hong, C., Geng, G., Li, H., Li, X., Peng, L., Qi, J., Yan, L., Zhang, Y., Zhao, H., Zheng,
785     Y., He, K., and Zhang, Q.: Trends in China's anthropogenic emissions since 2010 as the consequence of clean air actions,
786     Atmos. Chem. Phys., 18, 14095-14111, 10.5194/acp-18-14095-2018, 2018.

787     Zhong, J., Cai, X.-M., and Bloss, W. J.: Coupling dynamics and chemistry in the air pollution modelling of street canyons: A
788     review, Environmental Pollution, 214, 690-704, https://doi.org/10.1016/j.envpol.2016.04.052, 2016.

789     Zhong, J., Cai, X.-M., and Bloss, W. J.: Large eddy simulation of reactive pollutants in a deep urban street canyon: Coupling
790     dynamics         with         O3-NOx-VOC         chemistry,         Environmental         Pollution,         224,         171-184,
791     https://doi.org/10.1016/j.envpol.2017.01.076, 2017.

792     Zhu, Y., Zhan, Y., Wang, B., Li, Z., Qin, Y., and Zhang, K.: Spatiotemporally mapping of the relationship between NO2
793     pollution and urbanization for a megacity in Southwest China during 2005–2016, Chemosphere, 220, 155-162,
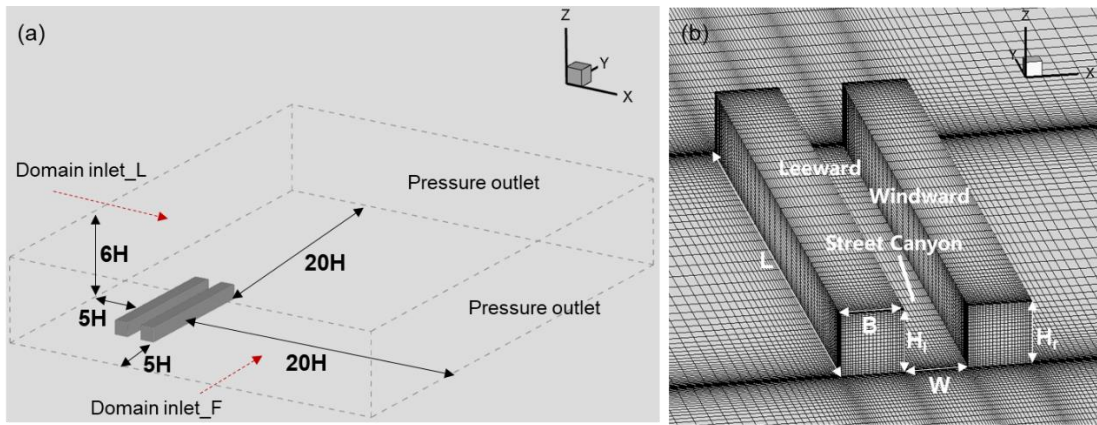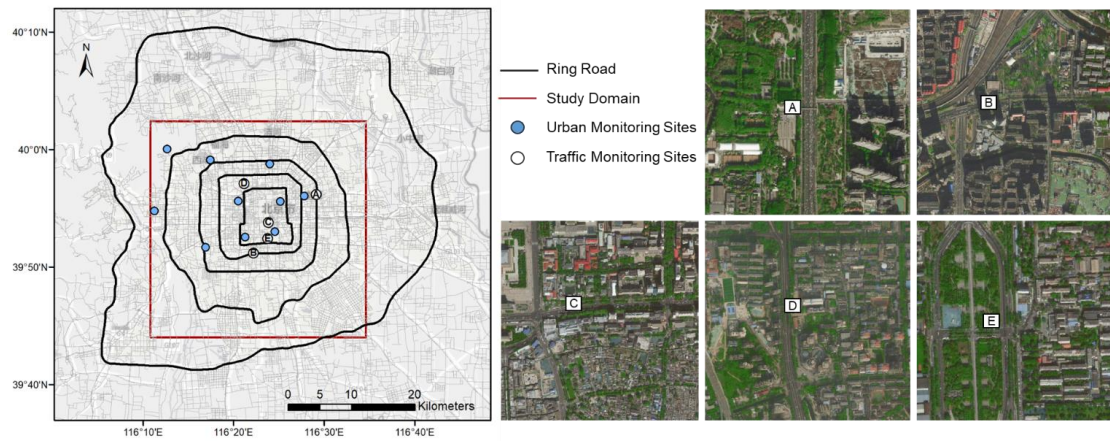794     https://doi.org/10.1016/j.chemosphere.2018.12.095, 2019.

795

796

797
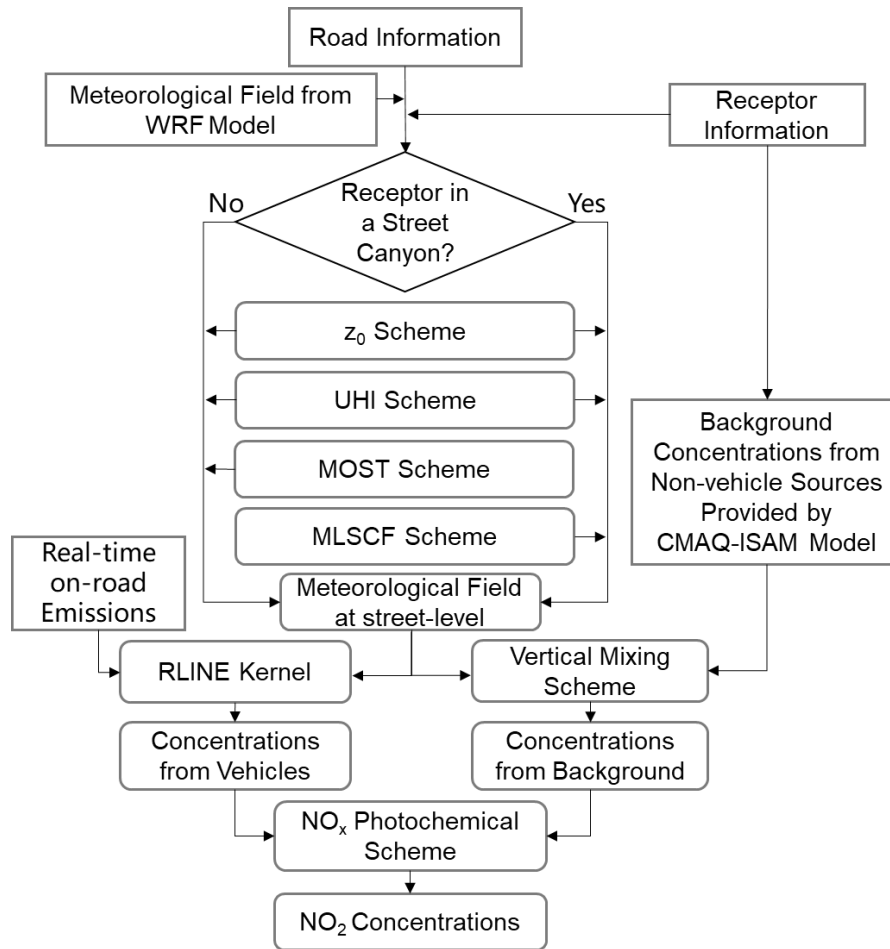


Figure 1: The framework of multiscale hybrid model CMAQ-RLINE_URBAN.

798

799

800

801
802  **Figure 2: Computational domain (a) and grid arrangement (b) in all CFD test case.**

803
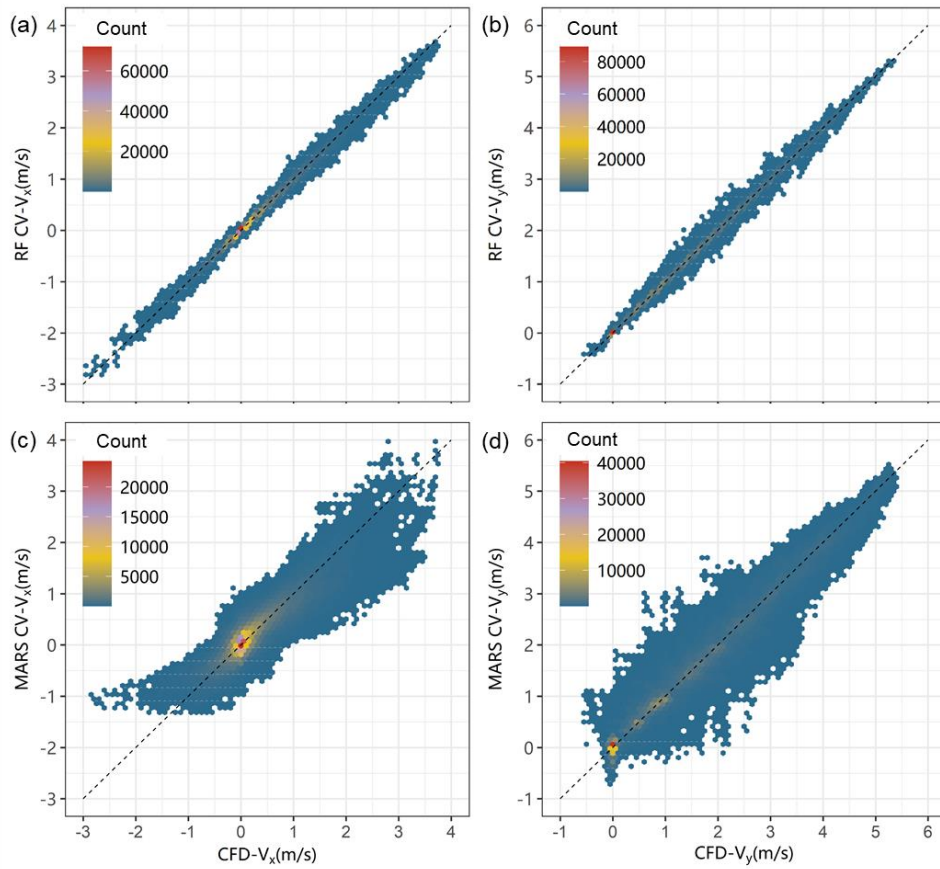804

805

Figure 3: Study domain (© OpenStreetMap contributors 2020. Distributed under the Open Data Commons

Open Database License (ODbL) v1.0) and location of monitoring sites (© Microsoft). A. DSH; B. NSH; C.
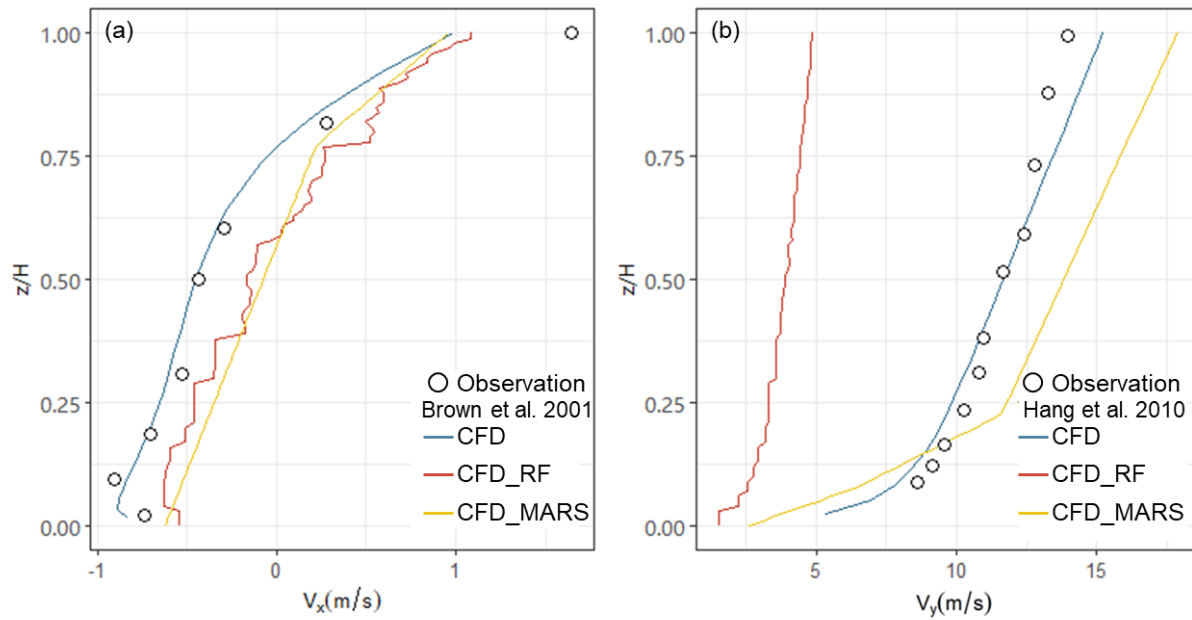
QM; D. XZM; E. YDM.

809

810
811 **Figure 4: Cross validations of machine learning models for Vx (a, c) and Vy (b, d): (a)-(b) RF model; (c)-(d)**

812 **MARS model.**

813

814
815 **Figure 5: Performances of machine learning on velocity profile in wind tunnel experiments. The street**

816 **canyon was perpendicular (a) or parallel (b) to the wind direction at the roof level in different experiments.**

817 **The detailed description of each experiment was introduced in Section 2.2.3.**

818
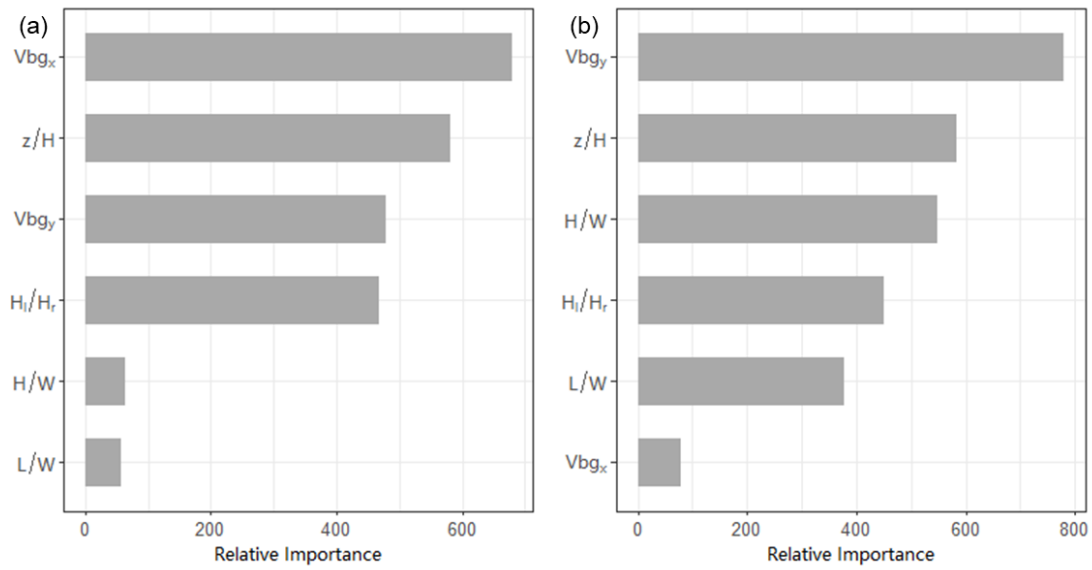
819

820 **Figure 6: Variable importance ranking in the RF model for (a) $V_x$ and (b) $V_y$.**

821
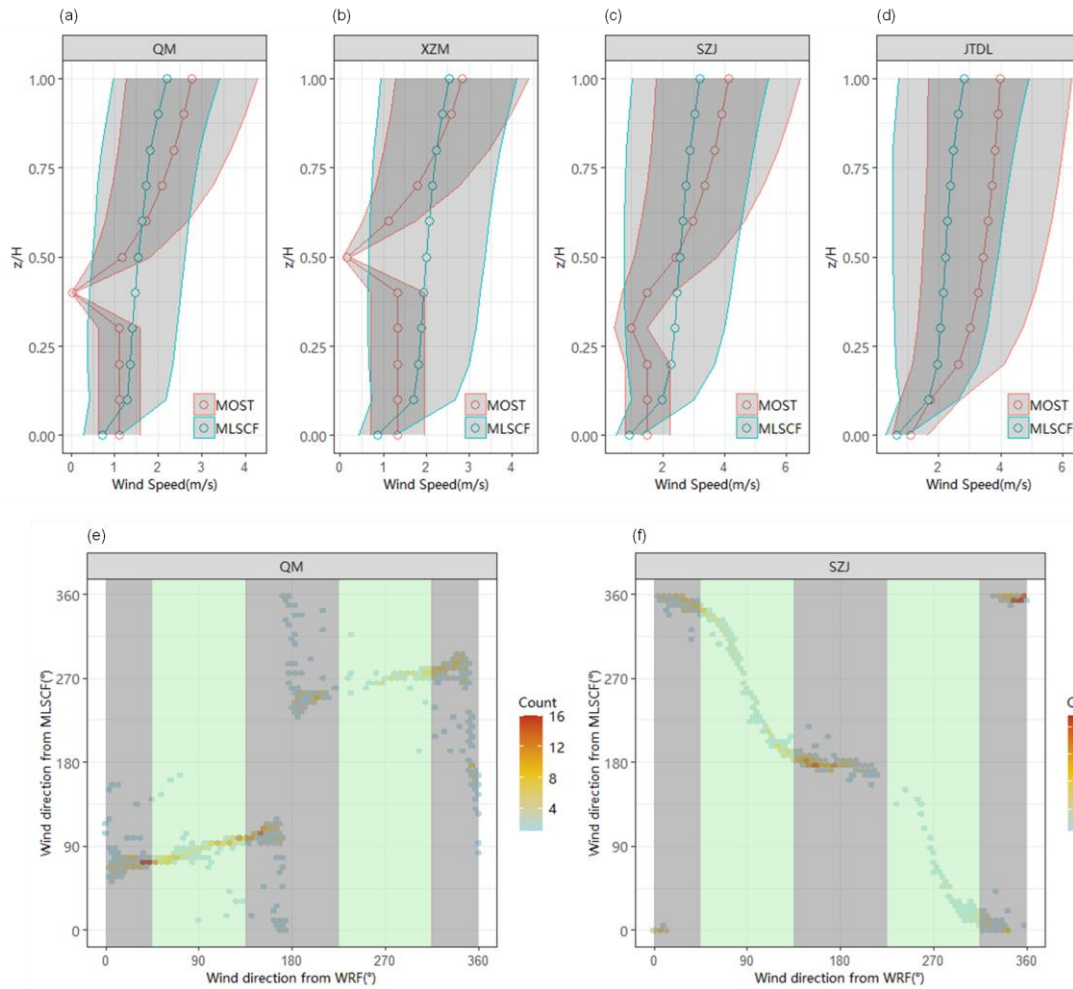
**Figure 7: Influence of MLSCF on wind filed in the street canyon. Monthly averaged vertical profile of wind speed from MOST and MLSCF method in different street canyons: (a) QM (H/W=0.22); (b) XZM (H/W=0.35); (c) SZJ (H/W=1); (b) JTDL (H/W=1.93). The gray shade represents the standard deviation in results of all hours. Hourly wind direction from WRF model (at roof level) and MLSCF method (at ground level) in different street canyons: (e) QM (H/W=0.22); (f) SZJ (H/W=1). As the gray and green shade shown, the background wind over the street canyon provided by WRF model was divided into four main directions: east, west, south and north.**
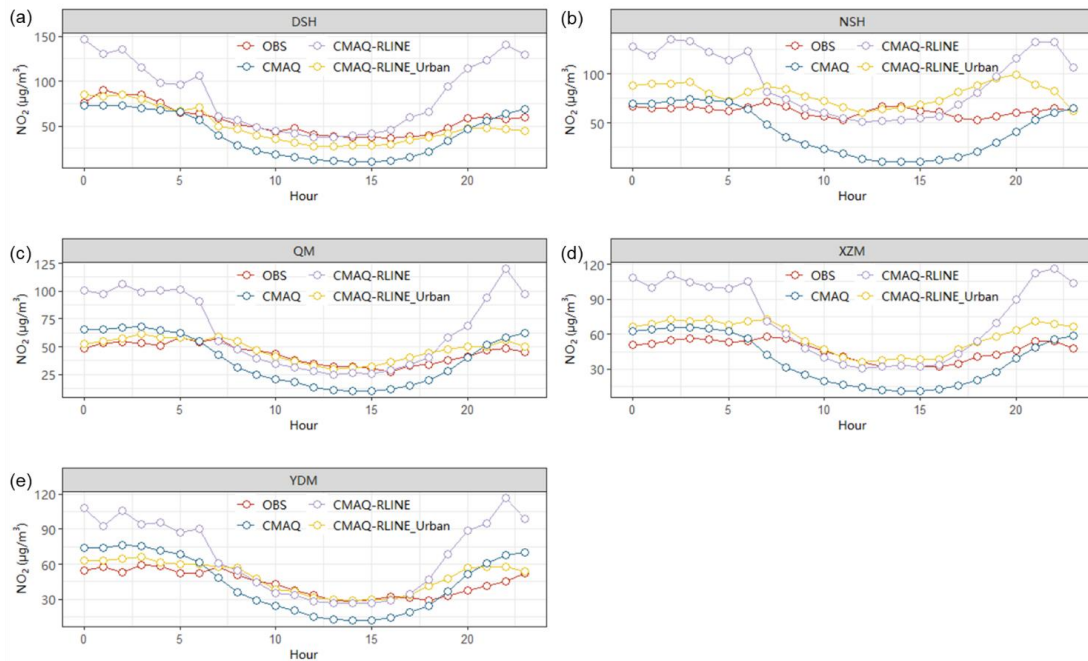
831
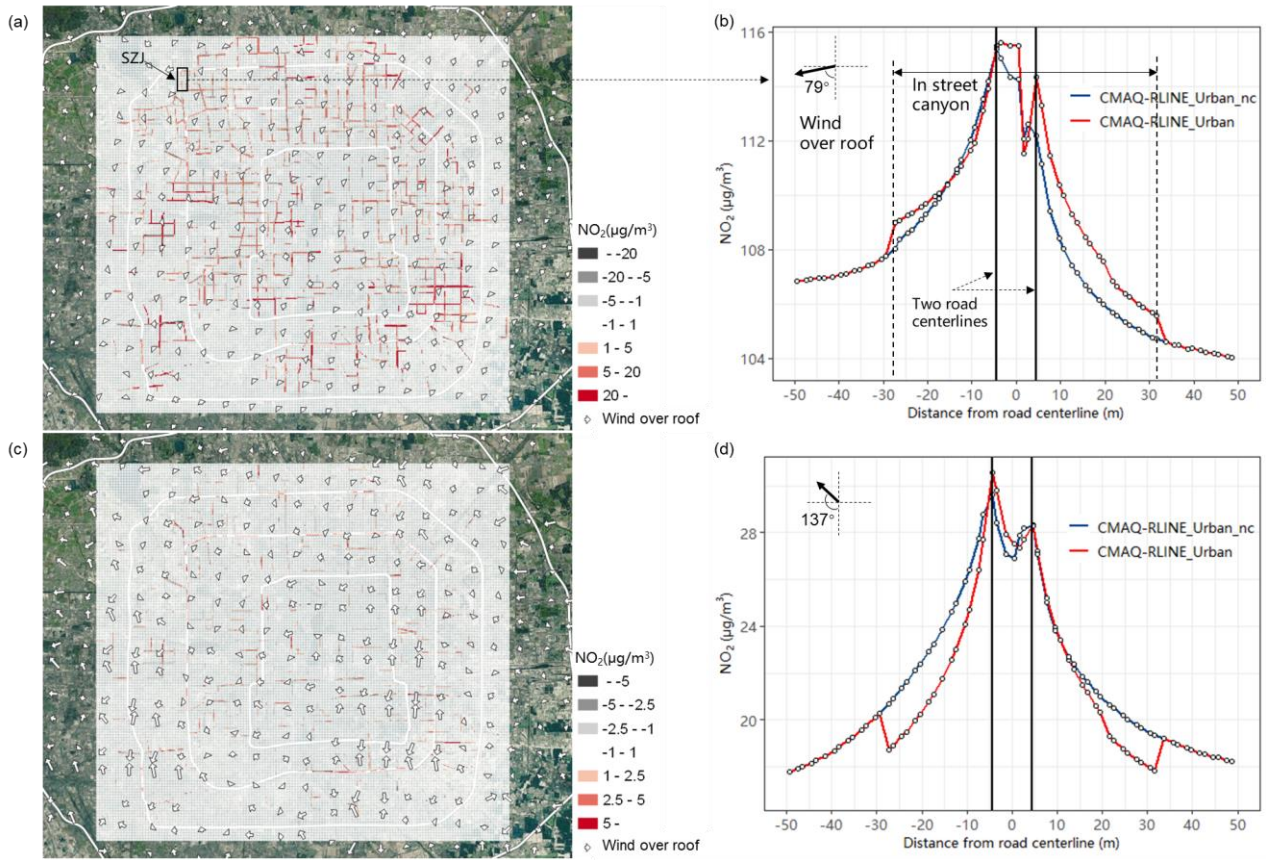
**Figure 8: Differences in NO₂ concentrations at the height of 1.5 m impacted by MLSCF scheme (a, c) over the study domain (CMAQ-RLINE_URBAN - CMAQ-RLINE_URBAN_nc) (© Microsoft) and (b, d) near SZJ in 2019-08-24 at 0:00-1:00 (a, b) and 10:00-11:00 (c, d).**

835

836

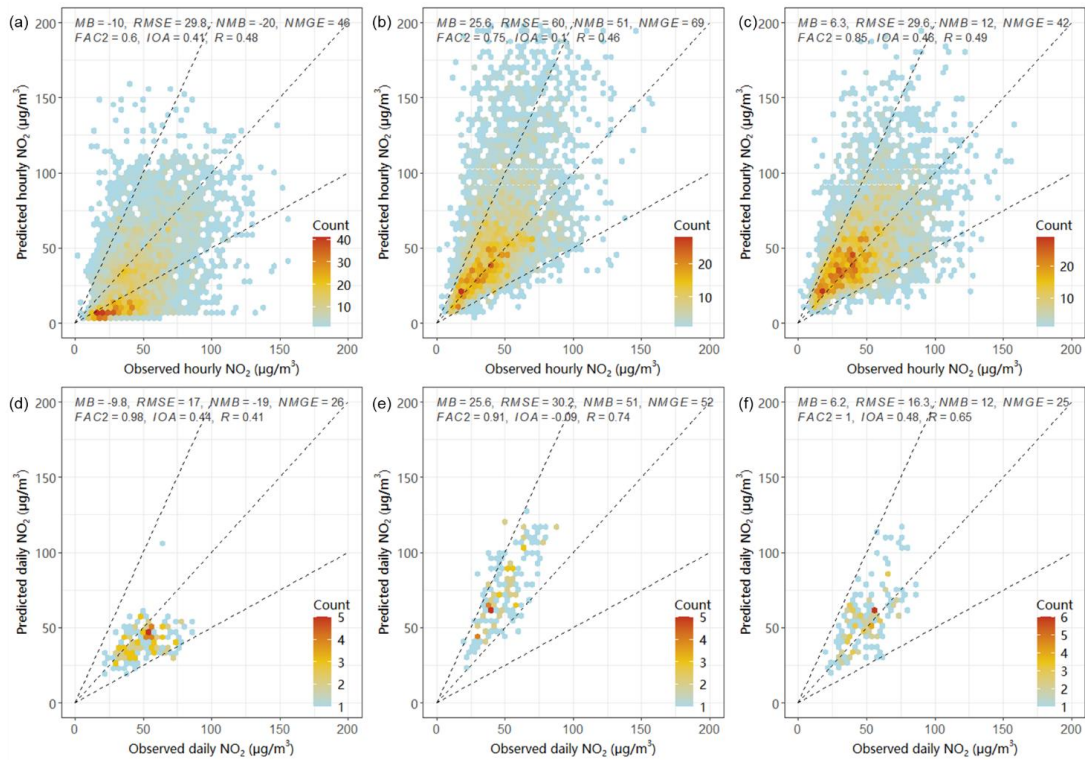**Figure 9: Diurnal variations of observed and predicted hourly averaged NO$_2$ concentrations from different**

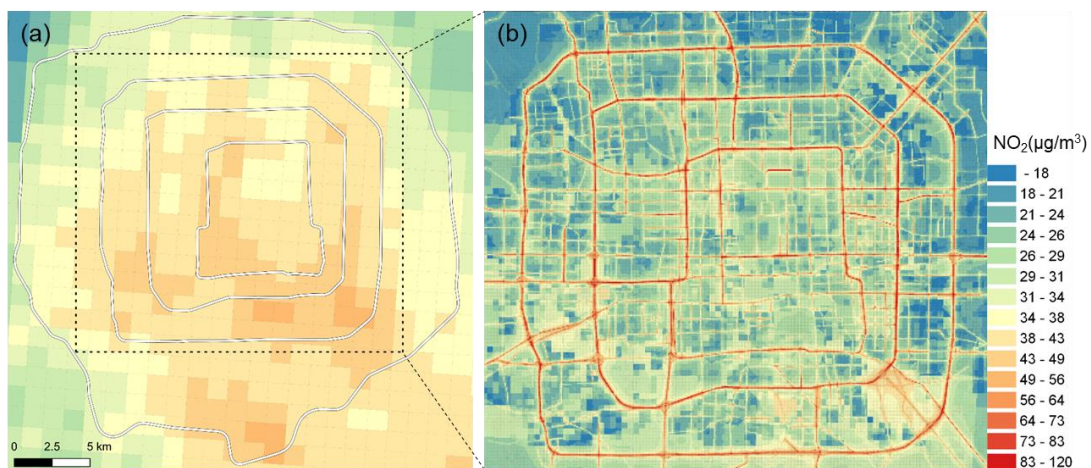**models at near-road monitoring sites: (a) DSH; (b) NSH; (c) QM; (d) XZM; (e) YDM.**

839

Figure 10: Observed and predicted hourly (a-c) or daily averaged (d-f) NO2 concentrations from different models at near-road sites: (a, d) CMAQ model; (b, e) CMAQ-RLINE model; (c, f) CMAQ-RLINE_URBAN model.

847
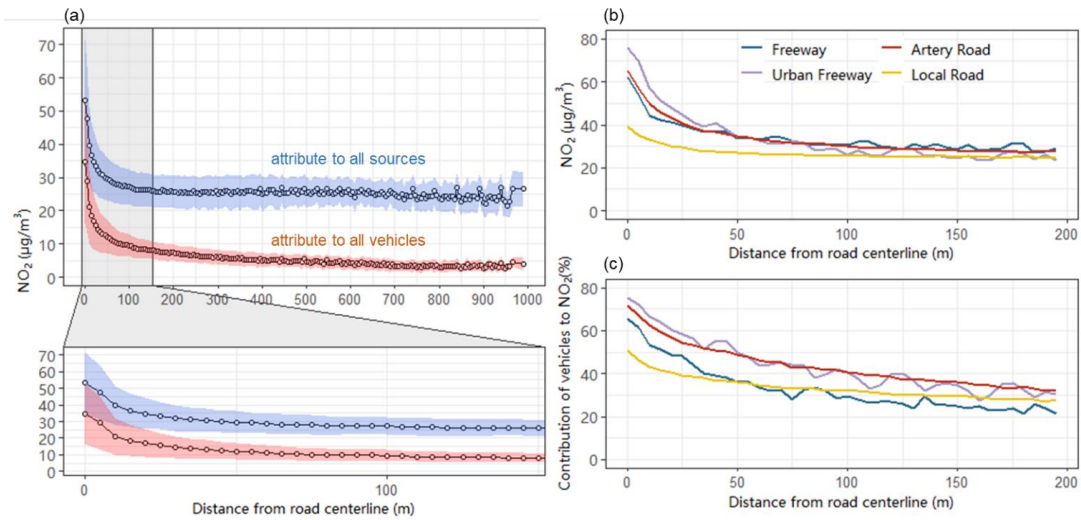**Figure 11: Spatial distribution of monthly averaged NO₂ concentrations from (a) CMAQ model and (b) CMAQ-RLINE_URBAN model (© OpenStreetMap contributors 2020. Distributed under the Open Data Commons Open Database License (ODbL) v1.0).**

851

Figure 12: Monthly averaged $NO_2$ concentrations attributed to all emission sources or vehicles with distance from the receptor to its nearest road centerline. (a) $NO_2$ attributed to all emission sources near all roads; (b) $NO_2$ attributed to all emission sources near different road types; (c) Relative contribution of vehicles to $NO_2$ near different road types. The shade area in (a) represents the standard deviation in results of all receptors.

858 **Table 1: Values of controlling factors used in the simulations.**

| Controlling factor | Value | | | | |
|---|---|---|---|---|---|
| $H_l/H_r$ (unitless) | 0.50 | 0.75 | 1.00 | 1.33 | 2.00 |
| $H/W$ (unitless) | 0.25 | 0.50 | 1.00 | 2.00 | - |
| $L/H$ (unitless) | 3 | 5 | 10 | 20 | - |
| $V(H)$ (m/s) | 1 | 2 | 3 | 4 | 5 |
| $\alpha$ (°) | 0 | 30 | 60 | 90 | - |

859
860

**Table 2: Model performances under different scenarios**

| Sites | Scenario | MB | RMSE | NMB | NMGE | FAC2 | IOA | *R* |
|---|---|---|---|---|---|---|---|---|
| | CMAQ | 3.1 | 25.6 | 9 | 53 | 0.65 | 0.45 | 0.52 |
| All | CMAQ-RLINE | 18.5 | 46.6 | 53 | 77 | 0.67 | 0.19 | 0.55 |
| | CMAQ-RLINE_URBAN | 4.6 | 25.8 | 13 | 49 | 0.75 | 0.49 | 0.57 |
| | CMAQ | 8.0 | 24.3 | 27 | 58 | 0.68 | 0.40 | 0.59 |
| Urban | CMAQ-RLINE | 12.3 | 35.8 | 43 | 76 | 0.64 | 0.20 | 0.50 |
| | CMAQ-RLINE_URBAN | 1.3 | 23.1 | 4 | 51 | 0.71 | 0.47 | 0.49 |

*MB: Mean bias; RSME: Root mean squared error; NMB: Normalized mean bias; NMGE: Normalized mean gross error; FAC2: Fraction of predictions within a factor of two; IOA: Index of agreement; R: correlation coefficient.